GROUND PENETRATING RADAR LOCATION OF BURIED AVALANCHE VICTIMS

A thesis submitted to the Faculty and Board of Trustees of the Colorado School of Mines in partial fulfillment of the requirements for the degree of *Master of Science* (*Geophysics*).

Golden, Colorado

Date 11/12/04

Signed:

Justin J. Modroc

Approved:

Professor Gary R. Oll oeft

Professor of Geophysics

Thesis Advisor

Golden, Colorado

Date 702 12, 2004

Signed: ______

Dr. Terence K. Young

Professor & Head

Department of Geophysics

ABSTRACT

Every year worldwide, over 150 people are killed by snow avalanches. The best way to survive being buried alive in an avalanche is with the use of requisite signal locator tools such as a personal transceiver or a RECCO[®] reflector (69% survival rate). If a person is buried without this equipment, search and rescue crews are limited to using rescue dogs (14% survival rate) or a probe line (12% survival rate) to locate the victim. Most of these methods have problems, including the RECCO system. Because of these problems, some victim's bodies are not recovered until the spring thaw. Since 1970, of all the avalanche fatalities in the United States (617), 6.3% of the victims have never been recovered using current search and rescue methods. Ground penetrating radar (GPR) should provide an effective method for locating buried avalanche victims. Snow is an excellent propagation medium (low loss) for GPR waves, and allows for deep penetration. A human body is comprised mostly of conductive fluid, which has a high contrast relative to snow, serving as an ideal reflection target for GPR. However, it was unknown how GPR will respond to the unfavorably changing dielectric properties as a body freezes. It is also unknown whether or not GPR can distinguish a human body from other natural and man made objects in the avalanche debris field. To answer these questions, I buried a human body mass equivalent (BME) in snow and recorded the GPR response and core temperature versus time, as the BME froze in a simulated avalanche burial at a cooperating ski area. Due to the similarity in properties to that of a human body, a freshly euthanized pig was used to represent the BME. The experimental measurements prove that it takes about 110 hours for the 66 kilogram (145 lbs) BME buried in snow to freeze completely with an ambient snow temperature of -6 °C. Throughout the course of the experiment, the BME could be uniquely identified relative to other buried natural and man made objects by its imaging GPR signature. Modeling

demonstrated this was a consequence of a unique waveform from constructive and destructive interference occurring in a thin layer sequence at the BME-air-snow interface. This resulted from initial body heat melting of snow, development of a thin air pocket, and subsequent refreezing. Thus, GPR has the potential to image, identify, and locate a human body, thereby saving lives, or at a minimum, help recover the body before spring thaw. However, there are several factors that are hindering this application; the lack of proper equipment and expertise, clothing and new materials may alter the GPR response, and not being able to identify the difference between a human and a deer or elk.

TABLE OF CONTENTS

ABSTRACT	• • • • • • • • • • • • • • • • • • • •	iii
TABLE OF C	CONTENTS	V
LIST OF FIG	GURES	vii
LIST OF TAI	BLES	ix
ACKNOWLE	EDGEMENTS	X
Chapter 1	INTRODUCTION	1
Chapter 2	GROUND PENETRATING RADAR	5
2.2 Theory	nction	5 6 10
Chapter 3	AVALANCHE BURIAL SIMULATION EXPERIMENT	17
3.2 Data A	cquisition	17 18 23
Chapter 4	RESULTS	27
4.1 Tempe 4.2 GPR . 4.2.1 V	rature	27

Chapter 5	MODELING.	• •	• •		•		•	•			•	•	•		•	•	•	•	•	•	•	•	•	49
	Waveform Model. tivity Analysis																							
Chapter 6	CONCLUSIO	NS.		•	•						•	•	•	•	• •				, .		, •			54
6.1 Discu 6.2 Futur	e Work															•								54 56
REFERENC	CES	• •	• •	• •	•	•	• •	•	• •	• •	•	•	•	• (•		•		•		•	•	58
APPENDIX																								62

LIST OF FIGURES

1.1	Telluride avalanche	1
1.2	Survival percentage versus burial time	2
2.1	Dielectric and conductivity of tissue vs. temperature and frequency	15
2.2	Dipole antenna radiation pattern	16
3.1	Simulation experiment line	20
3.2	Picture of line 1	20
3. 3	Picture of line 2	21
3.4	Target pictures and GPR direction of traverse	22
3.5	Processing steps and flow diagram	25
3.6	GRORADAR hyperbola fitting	26
3.7	Migrated 900 MHz data	26
4.1	Temperature data	28
4.2	Earliest GPR data 450 MHz and 900 MHz comparison	30
4.3	GPR data 450 MHz and 900 MHz comparison line 2	31
4.4	Latest GPR data 450 MHz and 900 MHz comparison	32
4.5	450 MHz data of natural and man-made objects	34
4.6	900 MHz BME trace	35
4.7	900 MHz target waveforms	37

4.8	450 MHz target waveforms	38
4.9	450 MHz BME waveforms	39
4.10	900 MHz BME waveform amplitudes vs. time	40
4.11	FFT waveform padding methods	42
4.12	FFT 450 MHz BME reflections	43
4.13	FFT 900 MHz BME reflections	44
4.14	FFT 450 MHz target reflections	45
4.15	FFT 900 MHz target reflections	46
4.16	Raw data trace emphasizing background noise	48
5.1	Full waveform model and input parameters	51
5.2	Graphic display of changing layered model	51
5.3	Full waveform 900 MHz model response	52
5.4	Full waveform 450 MHz model response	53
6.1	BME core temperature and normalized minima amplitude comparison	57

LIST OF TABLES

2.1	Electrical properties of relevant materials	11
2.2	Size of EM wavelength in relevant materials	12
2.3	EM reflection energy between different media	13
3.1	Target size and description	21

ACKNOWLEDGEMENT

I would like to recognize my advisor, Dr. Gary Olhoeft, who opened his door for this unique research and was accommodating to my athletic schedule. He also provided some partial funding. Partial tuition funding was provided by the Hui Oi-Chow fellowship and Dr. Olhoeft. The Society of Geophysics Graduate Students (SGGS) provided partial funding for a trip to present this research at the 2004 GPR conference in Delft, The Netherlands. There are several other people who need recognition, because without their help this research would not have been possible. First, Ron Kidder and Pip Baehler of the Loveland Ski Patrol were a tremendous and enthusiastic help. Secondly, Susan Smith of Cortemp® technology HQ inc. provided me with the temperature hardware at a discounted price. Thirdly, Dale Atkins and Halsted Morris of the Colorado Avalanche Information Center (CAIC) provided valuable avalanche statistics and information. Finally, I would like to thank David Stillman, Doug Klepacki, and Bruce Stott for all the field work help.

Most importantly I would like to acknowledge....

My noble father (Allen), loving mother (Bonnie), nurturing big brothers (Tony and Nick), and wonderful extended family and friends that supported my academic and athletic lifestyle. I would also like to thank my feline partner-in-crime "Montana Roo-ski". Last but not least, I would also like to thank my favorite Language Arts teacher for proof reading this thesis, thanks again mom!

Thank You Everyone!

CHAPTER 1

INTRODUCTION

Avalanche activity is a normal process of winter in the mountains. Some avalanches are triggered by unsuspecting outdoor activists and others are controlled like the avalanche in Figure 1.1, located outside of Telluride, CO.



Figure 1.1 Picture of a controlled avalanche in Telluride, CO. (Avalanche.org 7-23-02 photo by Eric Limon)

Avalanche deaths worldwide have been on the increase since the early 1990's. Based on recent yearly averages, the United States has 30 avalanche fatalities, compared to 150 avalanche fatalities worldwide (Atkins, 2004). In order to help save the buried victim, the first 30 minutes are the most crucial, after which the chance of survival drops below 50%, Figure 1.2 shows the relationship between survival percentages versus burial time (Atkins, 2004). Although rare, there have been several successful rescues of avalanche victims that have been buried for over 12 hours.

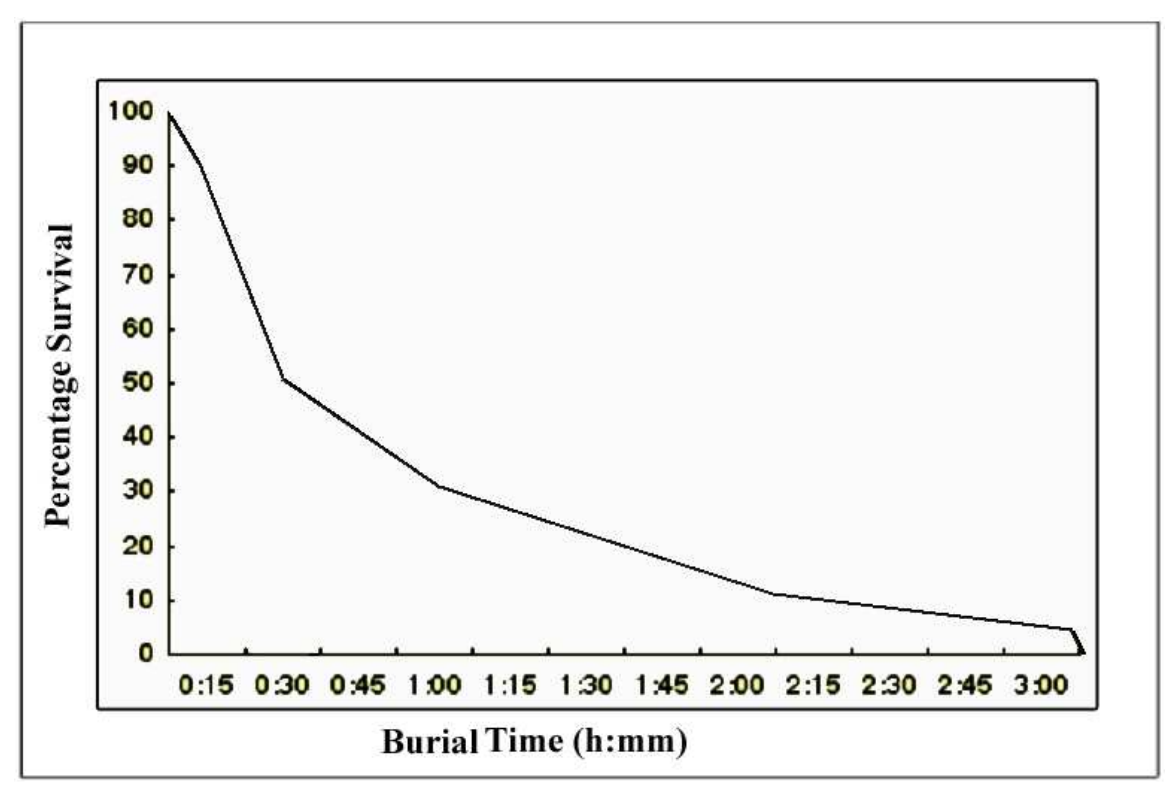


Figure 1.2 Graph representing the relationship between survival percentage and burial time (Atkins, 2004)

Currently, the best way to locate an avalanche victim buried with nothing sticking out of the snow is by a skiing companion using a special radio transceiver (avalanche beacon). Each individual's transmitter constantly transmits at 457 KHz and after one is buried, the surviving companion switches his transceiver to "receive" in order to pinpoint the buried transceiver and locate the buried person. The transceiver unit is compact, user friendly, and offers the best chance for surviving an avalanche burial. However, a majority of avalanche victims are not wearing transceivers, or can be lost or broken as the victim is buried. Another rescue method is the RECCO[®] Rescue System (Utzinger, 2002), popular in Europe. Clothing and other outdoor apparel are equipped with special reflectors, which double the frequency of the transmitted rescue signal to help pinpoint the victim's location. Search and rescue teams are deployed with the portable RECCO® antenna. The RECCO® method however, has had problems with too many reflectors in the search area. This is because the rescue personnel are typically wearing their outdoor gear, which may include a RECCO® reflector. The RECCO® system will only work with a direct line of transmission through the air and snow media. This means that the reflector is rendered useless if covered by the body, metal, or other debris. If the victim does not have the requisite equipment (or it is separated during the avalanche), the search and rescue team is limited to only two options, both of which can be flawed (McClurry and Schaerer, 1993).

The first, and faster option is the use of a specially trained rescue dog to sense the buried victim. However, the victim's scent can become contaminated if the area is searched by party members or rescuers prior to the dog's arrival (Utzinger, 2002). Another problem is rapid air movement, created from wind or an active helicopter, which will dilute and disperse the victim's scent. If the victim is completely entombed in snow, allowing no air flow to the surface, the dog's nose is rendered useless (14% survival). The final rescue option is the slow and methodical use of a probe line. This consists of a line of 3 to 20 people equipped with 2 to 3 meter long probe poles, systematically

probing the debris field together (Jamieson and Auger, 1997). These methods consume too much valuable time during the organization and actual probing, so survival drops to 12% or less (Atkins, 2004; Tremper, 2001). No search method or combination of methods work all the time. Due to the inadequacies of the current rescue methods, sometimes bodies are not recovered until the summer thaw. Since 1970, of all the avalanche fatalities in the United States (617), 6.3% of the victims were never found using current search and rescue methods (Atkins, 2004). A more efficient and reliable method is needed to help save lives and recover bodies.

Ground penetrating radar (GPR) could be a possible avalanche rescue tool to image and characterize avalanche debris and locate buried victims. In the early 1990's, a study was conducted to test the ability of using GPR to locate a human buried in snow pack (Niessen et al., 1994). This study failed to reach any conclusion as to whether or not GPR could be used to located buried avalanche victims. This could have been due to the study's poor simulation of an avalanche burial. In the study, a trench was dug in a regular snow pack and then a cave was dug into the snow. A person was put in the cave, and then measured with GPR. This was a poor simulation because the snow was not as dense and compact as avalanche debris, and it had not been melted and refrozen.

GPR has been used successfully to recover a victim from the aftermath of a deadly avalanche in the Swiss Alps in 2001 (Instanes et al., 2004). In this case, GPR was used to image and locate the victims that had been buried for over 6 days. This situation was ideal, with no trees or rocks in the avalanche debris to confuse the interpretation. Instanes et al. did not mention how much time or area the survey consumed.

CHAPTER 2

GROUND PENETRATING RADAR

2.1 Introduction

Ground penetrating radar (GPR) has been successfully used for characterizing the subsurface to solve many different problems (Olhoeft, 2003). Some current GPR applications include utility detection, groundwater studies, agriculture water content studies, archaeology, glaciology, and many more. GPR technology has the potential to solve many more problems where the answers are hidden in the subsurface.

When GPR data are collected along a 2D profile, they provide laterally spaced traces detailing the reflected energy from within the subsurface. This information is used to produce an image of a distorted cross-section of the subsurface. By utilizing and fully understanding the GPR system, some physical properties of the subsurface can be interpreted to provide a true cross-section.

GPR was first used to help characterize and study glaciers over 75 years ago. The very first published GPR survey was used to determine the depth of a glacier, reported in 1929 (Stern, 1929). The technology re-surfaced in the 1950's when planes began crashing into the Greenland ice sheet. The radar altimeter failed due to a lack of reflected energy from the air-ice boundary, and calculated a false altitude using the ice-ground boundary. This spawned a large increase in the use of GPR to image glaciers and ice sheets (Olhoeft, 1988). Since then, the number of applications for GPR has grown significantly, along with the information and knowledge gained from the data. As a new

application, GPR may be an effective tool for imaging avalanche debris. Search and rescue crews could possibly use GPR to help locate and rescue/recover buried victims.

It should be possible to effectively image a human body buried in snow utilizing GPR (Niessen et al., 1994; Yamaguchi et al., 1991; Annan, 2001; Page and Ramseier, 1975). It is widely known that snow and ice provide excellent propagation media for GPR waves (Achammer and Denoth, 1994). In snow, a human body, a highly conductive mostly liquid medium, serves as a high contrast reflector for GPR waves (Olhoeft, 1998). Hence, a human body buried in snow is an ideal GPR target. This large difference in contrast occurs due to changing dielectric properties of water (with temperature and phase change), and the conduction properties of the human body. If successful, this could be a potential life-saving application for GPR.

2.2 Theory

GPR utilizes electromagnetic (EM) wave propagation through the subsurface at frequencies ranging from megahertz (MHz) to gigahertz (GHz). Two antennas (a transmitter and receiver) are used to generate an EM pulse that propagates through the subsurface and record the scattered energy at the surface. Some of the propagating EM energy will be scattered (reflected) when it encounters a medium with contrasting electrical or magnetic properties. The reflected energy is measured by the receiver and is then sent to a computer to be saved and displayed in real-time. By moving the antenna along a 2D profile, lateral traces are grouped together to provide a distorted cross-section-like image of the subsurface. By understanding the interactions between the electric and magnetic fields and the geometry, the subsurface material can be characterized correctly, leading to a true cross-section image.

To help understand how GPR works, we start with charge motion caused by external forces, such as resulted from an electric field or a time varying magnetic field. This force results in motion of charge (straight or rotating) called a current, which creates

a magnetic field (Olhoeft, 1998). The change in charge velocity (acceleration or deceleration) results in electromagnetic radiation.

Maxwell's equations describe the interaction between electric and magnetic fields and the corresponding coupled process propagating as a three-dimensional, polarized, vector wave field, known as electromagnetic radiation (Balanis, 1989). The equations in vector form are

$$\overline{\nabla} \times \overline{\mathbf{E}} = -\frac{\partial \overline{B}}{\partial t};$$

$$\overline{\nabla} \times \overline{\mathbf{H}} = \overline{J} + \frac{\partial \overline{D}}{\partial t};$$

$$\overline{\nabla} \bullet \overline{\mathbf{D}} = q;$$

$$\overline{\nabla} \bullet \overline{\mathbf{B}} = 0;$$
(2.2.1)

where $\overline{\mathbb{E}}$ is the electric field strength vector [volt/m], $\overline{\mathbb{H}}$ is the magnetic field intensity vector [ampere/m], \overline{J} is the electric current density vector (flux) in [ampere/m²], \overline{D} is the electric displacement current vector in (coulomb/m²), \overline{B} is the magnetic flux density vector (tesla/m²), q is the electric charge density (coulomb/m³), t is time (s), and $\overline{\nabla}$ is the spatial vector derivative operator. Maxwell used these compact equations to describe how:

- 1.) A time varying magnetic field generates a current.
- 2.) An electric current gives rise to a magnetic field.
- 3.) Electric fields must form closed loops or terminate on a charge.
- 4.) Because there are no free magnetic charges, magnetic flux loops close on themselves.

These equations and relationships allow us to quantify the physical properties of materials using constitutive relationships. Electrical properties are broken up into two parts, charge transport and charge storage. Ohm's Law, a version of the diffusion equation, describes electrical charge transport through electrical conductivity.

$$\overline{J} = \sigma \overline{E} \tag{2.2.2}$$

where σ is the electrical conductivity [Siemens/m]. This equation describes charge motion and accounts for the conduction losses when dealing with EM energy. The electrical charge storage is described by charge separation (polarization).

$$\overline{D} = \varepsilon \overline{E} \tag{2.2.3}$$

In equation 2.2.3 ε is the dielectric permittivity [Farad/m]. This value divided by the dielectric permittivity of a vacuum ($\varepsilon_0 = 8.854 \times 10^{-12}$) is known as the relative dielectric permittivity. When an electric field is applied to a material, charges will separate until an internally generated electric field between the charges creates equilibrium. The amount of charge separated by an amount of distance is known as polarization and is storing energy. The ability of a material to support this phenomenon is known as dielectric permittivity.

The magnetic properties are described in the same manner as the electrical properties, except there is no equivalence to electrical conductivity. The following equation describes the magnetic dissipation and the storage.

$$\overline{B} = \mu \overline{H} \tag{2.2.4}$$

In equation 2.2.4, μ is the magnetic permeability [Henry/m]. This equation describes how intrinsic atomic and molecular magnetic moments respond to a magnetic field. Both the dielectric permittivity and magnetic permeability properties are complex, and frequency dependent.

The propagation of EM waves is controlled by several factors including geometry, and physical properties of the host medium: dielectric permittivity, magnetic permeability, and conductivity. Electrical and magnetic properties are described by complex quantities with real and imaginary parts describing storage and loss, respectively. Both the dielectric permittivity and magnetic permeability control the wavelength and velocity of the propagating EM wave. Conductivity represents energy loss by transfer to heat and attenuates the propagation of the EM wave, limiting depth of EM propagation.

EM waves are scattered (reflected, refracted, or diffracted) due to a change in material electrical and magnetic properties. The Fresnel reflection coefficient describes the impedance contrast at a change in electric or magnetic properties. The following equation (Balanis, 1989) describes the fractional amount of the energy that will be reflected (normal incidence) at the boundary of two contrasting mediums.

$$RC = \left(\frac{\sqrt{\frac{\mu_2}{\varepsilon_2}} - \sqrt{\frac{\mu_1}{\varepsilon_1}}}{\sqrt{\frac{\mu_2}{\varepsilon_2}} + \sqrt{\frac{\mu_1}{\varepsilon_1}}}\right)$$
(2.2.5)

Snell's Law is used to describe the angular dependence of scattering. It expresses how a wave front will change direction as it passes through the interface between media with different velocities. The Stokes and Mueller matrices are used to describe the polarization and corresponding changes. In some GPR surveys there is too much unwanted scattering; this is referred to as clutter.

The radar equation (Ulaby et al., 1982) describes how much power a receiving antenna will measure. The equation written in bistatic, free-space form is

$$P_{r} = P_{o}G_{t} \left[\left(\frac{1}{4\pi R_{t}^{2}} \right) \xi \left(\frac{1}{4\pi R_{r}^{2}} \right) \right] G_{r} \left(\frac{\lambda^{2}}{4\pi} \right)$$
(2.2.6)

where P_r (W) is the power received, P_o (W) is the power input to the transmitting antenna, G_t and G_r are gains applied to the transmitter and receiver antennas, respectively in the direction of the scatter, R_t (m) and R_r (m) are the distances from the scatterer to the transmitter and receiver respectfully, ξ (m²) is the cross-section of the scatterer, and λ (m) is the wavelength of the received energy. However, equation 2.2.6 is used for radar propagating through air looking for an aircraft. In order for this equation to be used for

GPR, material properties need to be accounted for. The radar equation for GPR (Powers, 1995) is

$$P_{r} = P_{o}G_{t} \left[\underbrace{\frac{1}{P'' \cdot P'}}^{A} \underbrace{\prod_{j=1}^{A} e^{-2\alpha_{j}r_{j}} K_{j}^{2}}_{j=1} \right] \underbrace{G_{r} \left(\frac{\lambda^{2}}{4\pi} \right)}^{C}$$

$$(2.2.7)$$

where A represents the spreading factor with both "in-plane" (P') and "out-of-plane" (P') spreading. B represents the loss due to material and reflection and transmission coefficients between the source, scatterer, and back to the receiver, where n is the number of segments in the travel path, α_j is the attenuation parameter of the jth segment, r_j is the distance along the jth segment, and K_j represents the complex relection or transmission coefficient associated with the jth segment, all as functions of frequency. C represents the effective aperture of the antenna (Powers, 1995). Equation 2.2.7 describes the power received as a function of the power input into the transmitter, and is a product of many important variables including; antenna properties, coupling and rough surface scattering, geometric spreading, exponential loss, and scattering properties. For detailed derivations please see Powers (1995) (note, his equation has a typo with a square missing).

2.3 GPR and Avalanche Debris Imaging

By utilizing and analyzing GPR theory, it may be possible to determine if GPR could be used to successfully image through avalanche debris and locate a buried victim. In order to determine this, the physical properties of relevant materials must be known (Table 2.1). The magnetic permeability of relevant materials is assumed to be that of free space and will henceforth be neglected. For a complete list of various body parts and their corresponding electrical properties see Gabriel and Gabriel (1996) and Durney et al.

(1986). The electrical properties of all other materials listed are from Annan (2001) and Frolov and Macheret (1999).

Table 2.1 Case specific material dielectric permittivity and conductivity

Material	Relative Dielectric Permittivity (ε_r)	Conductivity (mS/m)
Snow	2 to 12	0.00
Ice	3 to 4	0.01
Air	1.0	0.00
Fresh water	80.0	0.03
Rock	5 to 10	.01 to 2
Wood	8 to 15	0.02
Body	50.0	800.00

The relative dielectric permittivity of snow varies from 1.2 to 12.0 depending on several factors, including the amount of moisture, density, grain size and shape, age, temperature, and frequency (Achammer and Denoth, 1994 and Shivola, 1999). This low permittivity value is ideal for the propagation of EM waves, along with low conductivity. Snow has low conductivity losses, no relaxation losses (at the MHz frequency range), and low scattering losses (avalanche debris is relatively homogeneous). These low loss combinations allow for deep EM penetration making snow an ideal host medium for using GPR.

As a GPR target, the average human body has a relative dielectric permittivity of 50, this was determined using a weighted average of the five main human body components: skin, bone, blood, organs, and fat (Gabriel and Gabriel, 1996; Durney, 1986). Notice that the permittivity values for other materials that might be present in avalanche debris (rocks, wood, etc.) range from 2 to 12, which is similar to the values for snow. Using equation 2.3.1 (Powers, 1995), and assuming low loss (less than 30 mS/m) and nonmagnetic materials are present, it is possible to determine the wavelength (λ) from the

Table 2.2 provides the size of wavelength, computed from equation 2.3.1 for different frequencies in different media.

Medium	$\epsilon_{\rm r}$	Frequency (MHz)	Wavelength (m)	Resolution (m)
Dry Snow	2	450	0.47	0.16
Wet Snow	12	450	0.21	0.07
Air	1	450	0.67	0.22
Dry Snow	2	900	0.24	0.08
Wet Snow	12	900	0.11	0.04
Air	2	900	0.33	0.11

relative dielectric permittivity of the medium (ε_r), the desired frequency (f), and the speed of light (c) which is $3x10^8$ [m/s] in a vacuum. Table 2.2 shows the size of wavelength and resolution for different frequencies in three relative media.

$$\lambda = \frac{c}{f \times \sqrt{\varepsilon}} \tag{2.3.1}$$

In order for GPR to resolve a target, a piece of the target needs to be at least one third of the EM wavelength (Olhoeft, 2003). Table 2.2 shows that commonly available 450 MHz and 900 MHz GPR frequencies are both capable of resolving a body buried in snow regardless of its orientation. In ideal conditions, with sufficient contrast, it is possible to resolve a target that is only one tenth of the EM wavelength.

Using the Fresnel reflection coefficient and equation 2.2.5 it can be determined what fractional amount of energy will be reflected at the boundary of two contrasting media. Table 2.3 shows the theoretical fractional amount of energy that will be reflected due to contrasting dielectric permittivity values.

It is important to note that the RC size is much smaller for natural objects relative to the human body and man-made objects with metal. It may be possible to distinguish targets buried in snow based on the amplitudes of the recorded GPR reflections. However, it has been shown (Gabriel and Grand, 1985) that when body tissues are cooled below freezing their dielectric permittivity values drop with the temperature. Therefore, it is unknown whether a frozen body will provide enough contrast to be imaged and recovered using GPR.

In the past, there have been tests on the dielectric permittivity of super cooled tissues (Gabriel and Grant, 1985). Their results showed that the dielectric permittivity and conductivity of ocular tissue had steadily decaying values from 20° C to -9° C. At -9° C a sharp transitional drop occurred for both values. This experiment only used one type of tissue and is not representative of a whole body. It does however, suggest that if a body core temperature drops below -9° C, it may not provide sufficient contrast from the avalanche debris medium to be distinguishable using GPR.

Figure 2.1 is from Gabriel and Grant (1985), and shows the relationship between temperature, dielectric permittivity and conductivity of retina tissue versus frequency.

Table 2.3 provides the theoretical fractional amount of reflected energy at media boundary.

	RC	RC
Medium	ε (Dry snow) = 2	ε (Wet snow) = 12
Air	-0.20	-0.50
Rock	0.27	0.13
Fresh Log	0.39	0.10
Body	0.64	0.34
Metal	1.00	1.00

^{*}The snow media were evaluated as the first medium.

In the MHz range, we see that there is little temperature dependence on the dielectric permittivity. However, there is a significant change in the MHz range for conductivity varying with temperature. This can have a negative effect on the amount of contrast between a body and snow.

Another important issue is the antenna radiation pattern. Figure 2.2 (Powers, 1995) shows how a dipole antenna will typically radiate in different dielectric media with zero conductivity. This is a good parallel to avalanche debris which has zero conductivity and a permittivity near 4. This Figure shows that a snow medium provides a wide radiation pattern for GPR energy that is ideal when searching for a buried target.

To help prove if GPR could be used as an avalanche rescue/recovery imaging system the following fundamental questions need to be answered. How will GPR respond to a freezing body? How long will it take for a body to freeze while buried in snow? Will it be possible to distinguish a body from other anomalies found in avalanche debris?

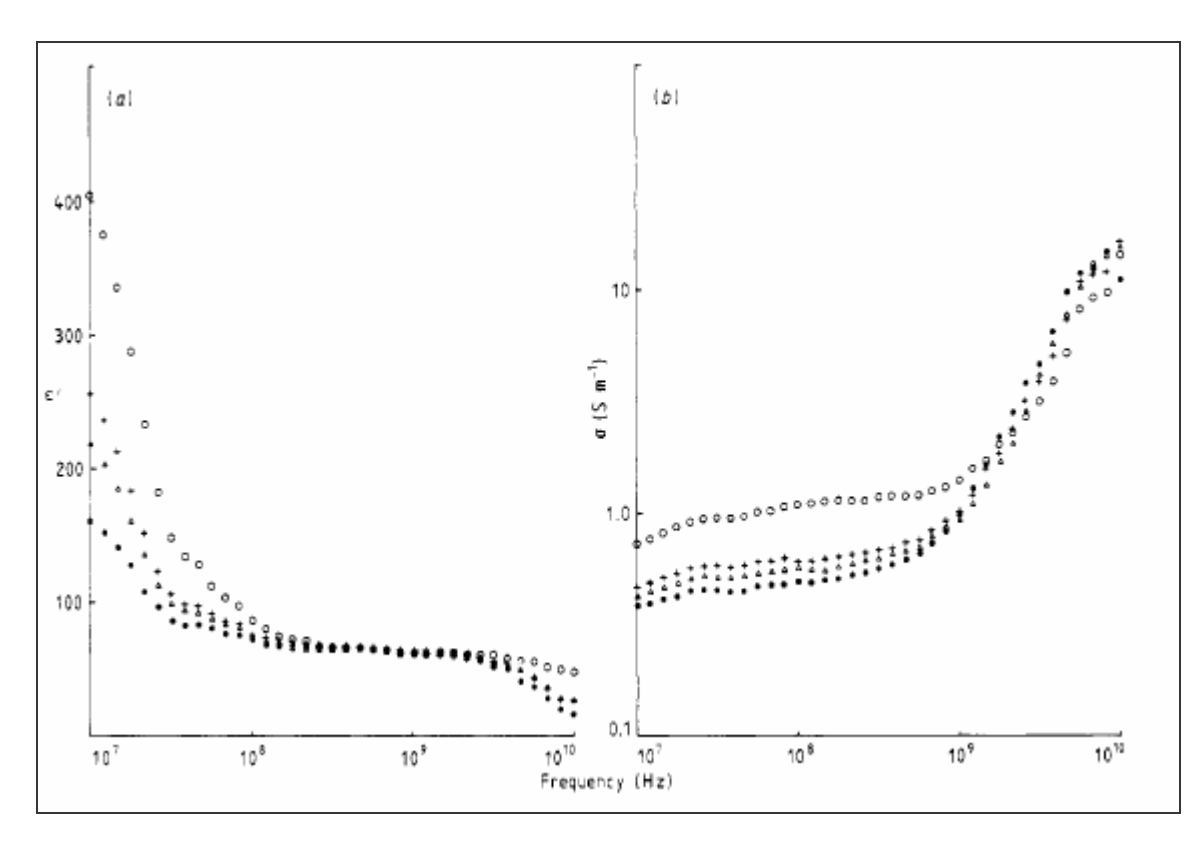


Figure 2.1 (a) Permittivity and (b) conductivity of retina at 20 (o), 1 (+), -1 (Δ), and -9° C (\bullet) (Gabriel and Grant, 1985).

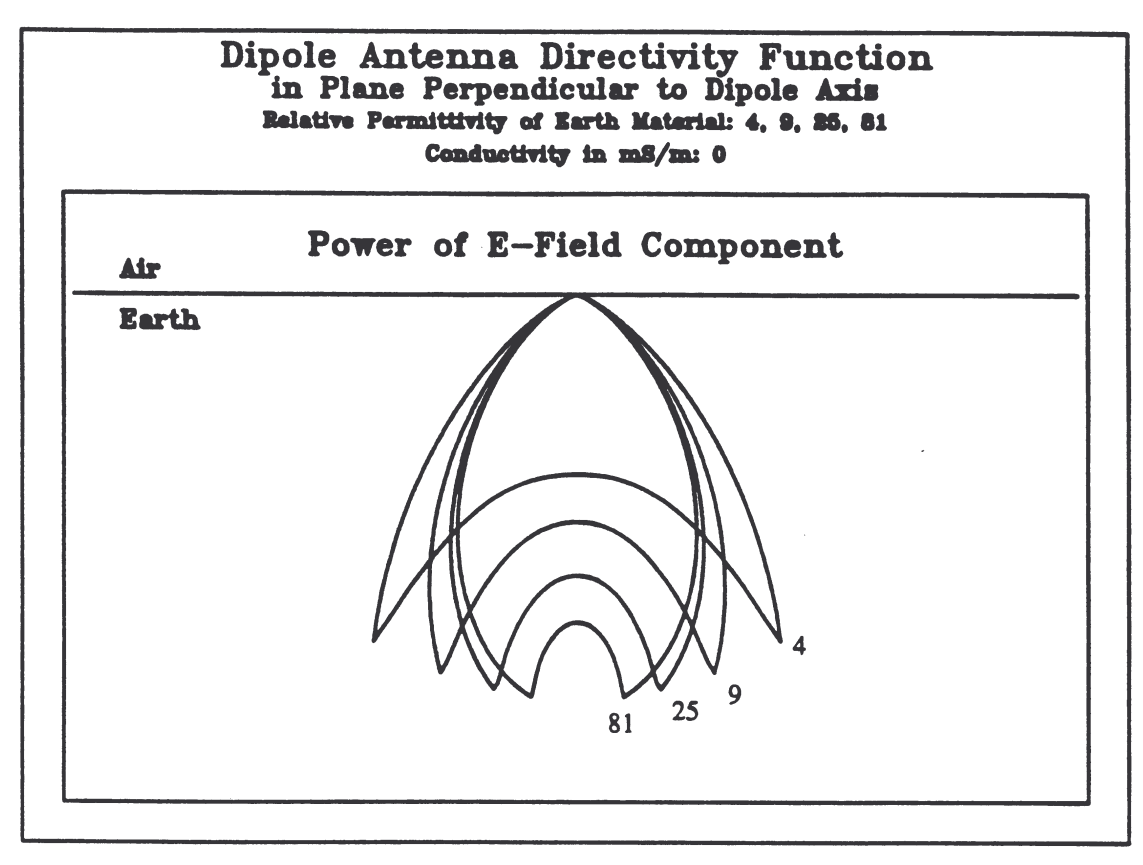


Figure 2.2 The perpendicular radiation pattern of a horizontal electric dipole on the ground surface is modified by the electromagnetic parameters of the ground. The patterns shown are for ground permittivities of 4, 9, 25, and 81, with ground conductivity equal to zero. Lower permittivity leads to a wider radiation pattern (Powers, 1995).

CHAPTER 3

AVALANCHE BURIAL SIMULATION EXPERIMENT

3.1 Introduction

To help determine if GPR could be used as a rescue/recovery imaging system, an experiment was designed to simulate the environment of an avalanche burial. A human body mass equivalent (BME) was buried in snow to simulate the buried victim. The BME's core temperature and GPR response were measured over time as the BME froze. Also, a database of GPR responses to natural and man-made objects was acquired.

Loveland Ski Area (CO, USA) cooperated by providing a location for the test, where they consolidated snow from plowing their parking lot. The experiment took place November 21-25, 2003.

In order to simulate the human body, the BME needed similar electrical and thermal properties. Pigs have been used for xenotransplantation of organs into humans (Appel et al., 2001; Wolf et al., 1997) because they have similar physiological properties to the human body. A common Yorkshire cross swine was used in this experiment. The Yorkshire family is Suidae, the genus is Sus, and the species is known as the Sus Scofa. Colorado State University's (CSU) regulations were followed regarding animal research due to the absence of any such regulations at the Colorado School of Mines. In accordance with CSU's Animal Care and Use Committee (ACUC), a pig destined for slaughter was intercepted between auction and butcher. A veterinarian then euthanized the pig; one hour later the experiment began with the burial of the pig in snow. The BME weighed approximately 66 kilograms (145 lbs), was 1 meter long, and 60 centimeters tall.

Appendix D contains the documentation associated with purchasing the Yorkshire swine and approval from CSM.

3.2 Data Acquisition

To measure the core temperature of the BME, a specially designed thermometer pill (CorTemp Technology® HQ Inc. Palmetto, FL) was made for the BME to swallow prior to euthanization. The pill contains an oscillating crystal sensitive to temperature. The pill transmits the crystal's signal to a nearby receiving unit operating at 252 KHz.

On Friday, November 21st, the BME was legally purchased and then euthanized by a veterinarian. The BME was buried in the deepest part of the snow pile. There was 0.9 meter (3 feet) of snow under the BME and roughly 0.76 meter (2.5 feet) above it. The BME was placed on its side with the GPR traverse orientated along the long axis of the body. Once buried, a GPR test line was created directly above the BME. Figure 3.1 shows a photo of the survey line. The beginning of line (BOL) and end of line (EOL) are annotated along with the corresponding target burial locations.

A Sensors and Software Pulse-Ekko 1000 GPR unit from the Colorado School of Mines, Department of Geophysics was used to acquire the data using two different ground coupled antennas: 900 MHz and 450 MHz. Most GPR measurements were collected using the 900 MHz antenna; the 450 MHz antenna was used less frequently as a complement. The first measurements were gathered at 110 minutes (900 MHz) and 121 minutes (450 MHz) after burial. Data was collected using a 30 nanosecond two-way travel time window in continuous mode with one stack; with in each trace, a data point was gathered every 50 picoseconds. The test line had fiducial markers every three feet to ensure accuracy of the survey geometry. A smoothed track the width of the GPR antennas was made to ensure that the same line was mapped with each repetition and to achieve maximum coupling with the snow. Figure 3.2 shows a picture of line 1 with fiducial markers and track. A metal plate was buried near the BOL for calibration purposes. Two

different test pits were located near the EOL, which hosted several different natural and man-made objects.

For the first 16 hours, a GPR measurement was made every half hour. The GPR measurement rate was then changed to one every hour. Problems did arise and staying consistent on the hour proved almost impossible due to blown fuses, cold and damp equipment (during a blizzard), and cold batteries (at night).

The test line evolved as the experiment aged. The first major change occurred at 11 hours after burial. At this point, the BOL was extended to separate the calibration plate from the BME. The EOL was also extended to accommodate the burial of different natural and man-made targets to obtain their GPR signatures.

A second line was added at 47 hours after burial. This line was perpendicular to and intersected line 1 directly above the BME, depicted in Figure 3.3.

The buried targets in the experiment include the following: square metal plate, BME, rock, dirt clod, ski boot, shovel, ski helmet, backpack, ski pole, ski, a freshly cut tree shrub, and log. Table 3.1 gives a description and dimension of each item and Figure 3.4 provides a picture of each target and the direction of GPR traverse, some are pictured with a glove for scale. Most of the targets were orientated such that maximum scattering was achieved with the GPR.

Approximately 50 different GPR measurements were collected using the 900 MHz antenna versus time, while there were only about 20 GPR measurements using the 450 MHz antenna. See Appendix A for all GPR data and a detailed list of GPR measurements and time schedule (*GPR measurements vs time.xls*).

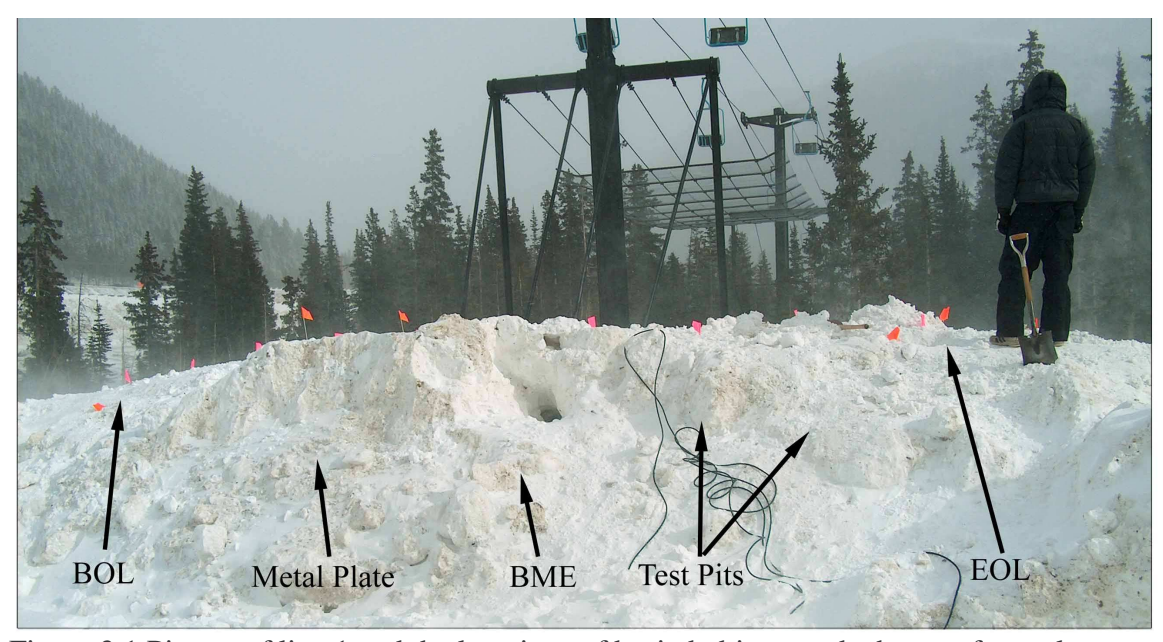


Figure 3.1 Picture of line 1 and the locations of buried objects and a human for scale.

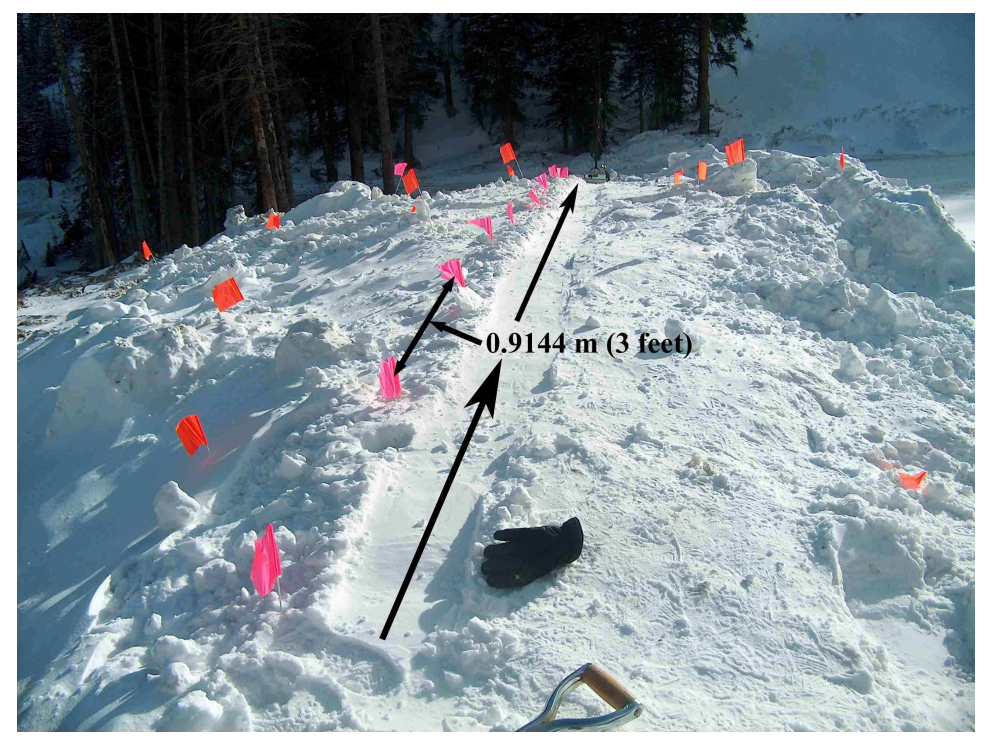


Figure 3.2 Picture of line 1 with fiducial flags every 0.914 m (3 feet) and antenna track.

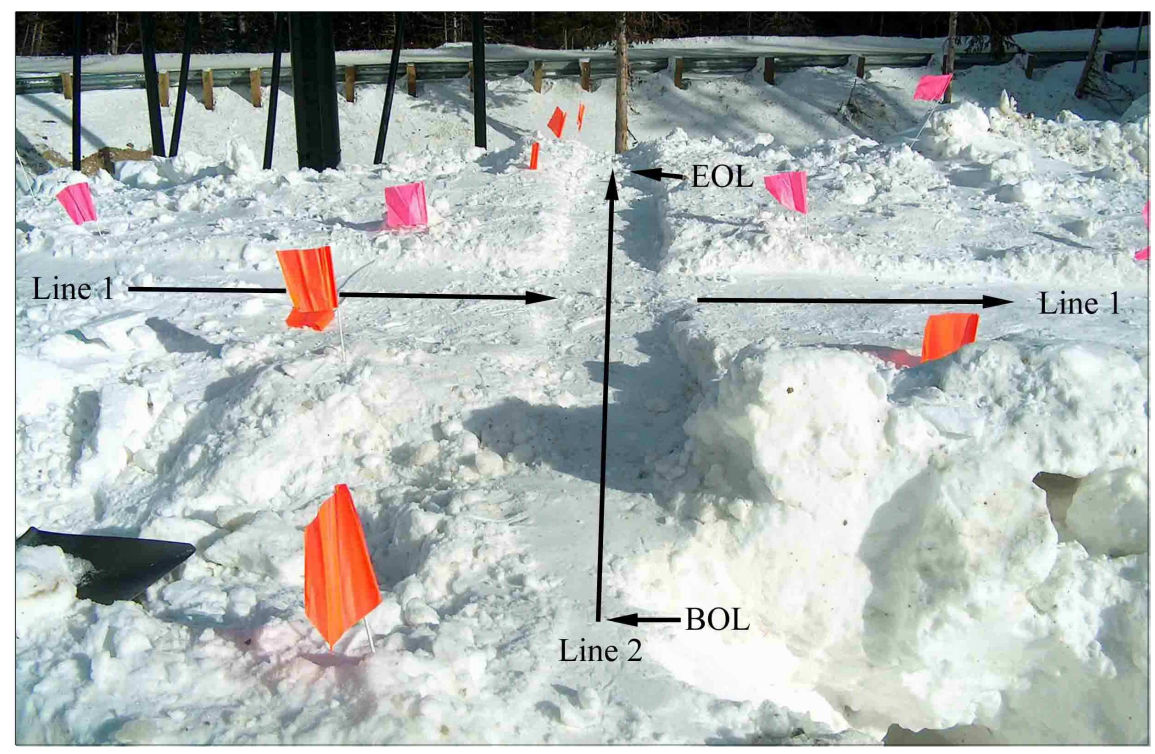


Figure 3.3 Picture of line 2, perpendicular to line 1.

Table 3.1 provides the dimensions and brief description for each target.

	Target	Dimensions (cm)	Description
1	Metal Plate	38x43x.2	Metal
2	BME	102x42x38	Biological Tissue
3	Rock	30x18x8	Granite
4	Dirt clod	7x13x7	Soil
5	Ski Boot	38x15x10	Plastic with some metal
6	Shovel	19x14	Metal
7	Ski Helmet	15x15x15	Plastic
8	Backpack	61x38x38	Fabric with some metal
9	Ski Pole	52x1x1	Metal
10	Ski	180x56x2	Metal and some plastic
11	Tree	76x41x41	Freshly cut wood
12	Log	61x8x5	Freshly cut wood

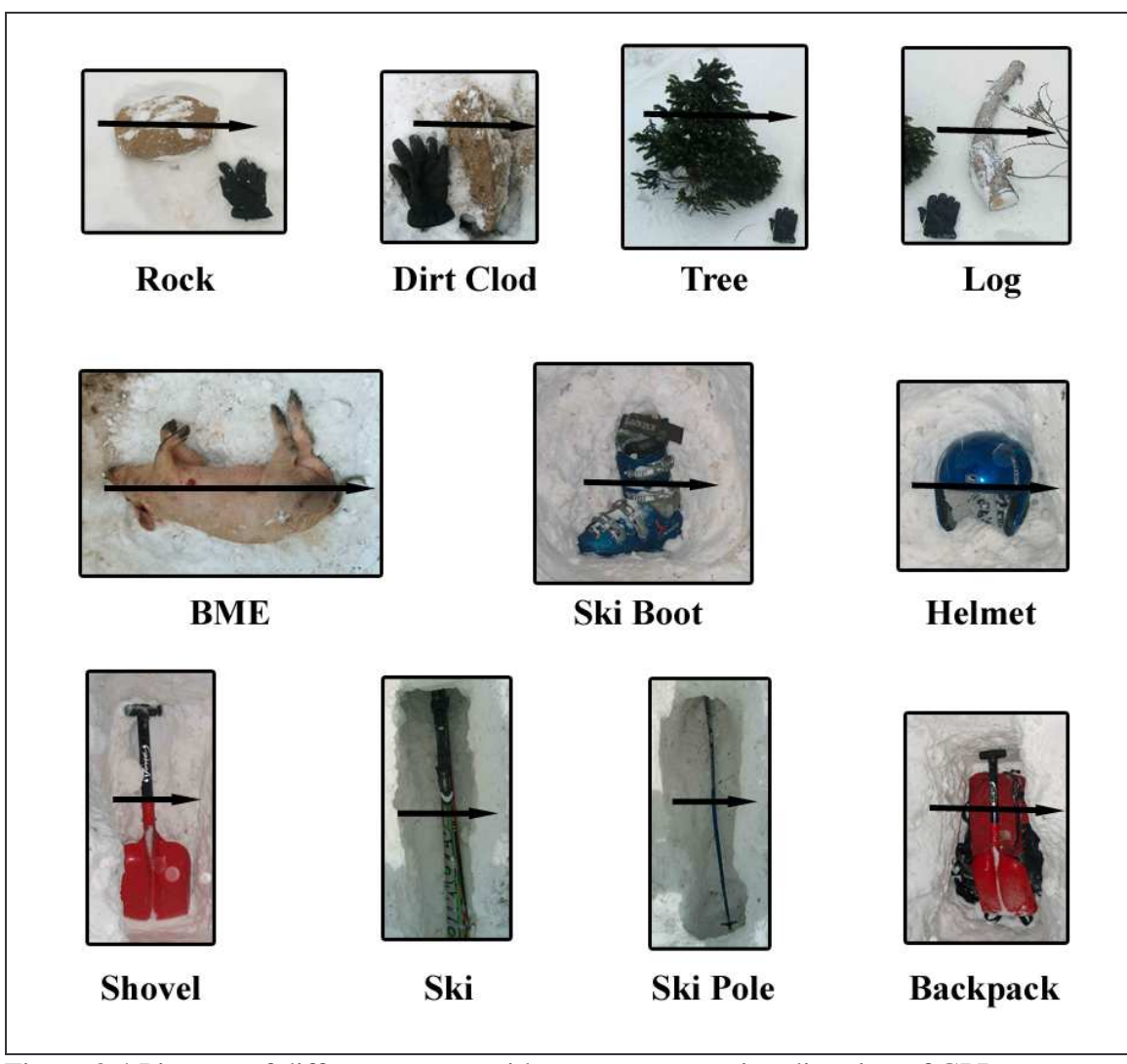


Figure 3.4 Pictures of different targets with arrow representing direction of GPR traverse along line 1. For line 2, the direction of GPR traverse across the BME is perpendicular to the direction of line 1.

3.3 Data Processing

A small percentage of GPR lines had bad traces that needed to be removed prior to processing. The trace removal was performed using the acquisition software for the Pulse-Ekko 1000 GPR system. The GPR data were processed using GRORADAR software (version 2003.11). All of the GPR data was minimally processed. See Figure 3.5 for a flow diagram and examples of how each step affected the data. The first step was to set the zero time. This was set to the location of the first recorded energy from the direct arrival. Next, a rubber sheet geometry correction was applied to the fiducial markers in the data. This was performed to account for variations in GPR traverse speed while collecting data. The third step was to set the permittivity of the medium (2.3) to get the correct velocity and corresponding depth. Figure 3.6 illustrates how this was found by fitting a curve to the hyperbola generated from the GPR reflections of the ski pole.

The fourth step was to apply a uniform gain across the entire range (30 ns). During the summer of 2004, a total distance measurement survey was conducted at the survey site in the Loveland parking lot. Using multiple photos from the November' 03 survey, the approximate location of the test line was marked out. With help from the local ski patrol, the relative elevation change of the parking lot along the line was measured. These data were then added to the snow depth thickness and turned into an electronic distance measurement (EDM) file. The final processing step was to use the EDM file to provide a topography correction to the data. Once the data were corrected for topography, the hyperbola velocity matching was performed again for a more accurate result.

Determining the correct velocity/permittivity was an iterative process between the hyperbola velocity matching and the topography correction. Eventually, a permittivity value of 2.3 was chosen. Figure 3.7 is an example of migrated GPR data. It shows that the correct velocity was chosen, with the collapsing of the hyperbolas in the data. Look closely at the BME, and notice how the hyperbolas have collapsed. Some of the data is

over migrated, which was due to changes in homogeneity of the snow and the curved GPR antenna surface.

Once all processing steps were completed, an encapsulated postscript file (EPS) was output from GRORADAR and opened using Adobe Photoshop (version 7.0) software to annotate and make the Figures ready for publication.

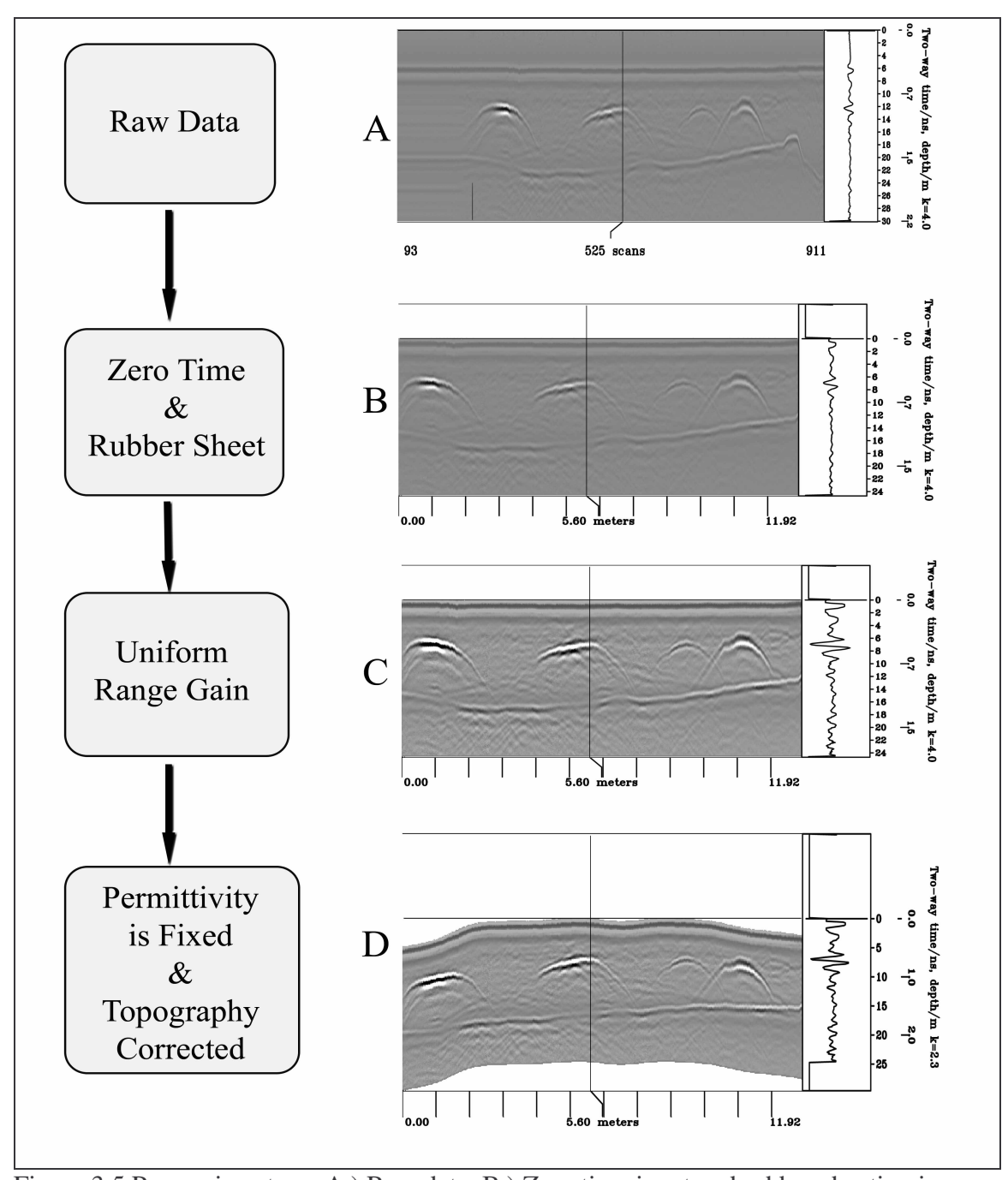


Figure 3.5 Processing steps; A.) Raw data, B.) Zero time is set and rubber sheeting is applied, C.) Gain is applied, D.) Topographic correction and correct permittivity are applied. For the final GPR data, the x-axis is the distance traversed in meters. The y-axis is the two way travel time in nanoseconds and also the depth in meters ($k = \varepsilon_r = 2.3$). The solid vertical line at 5.6 meters is a single wiggle trace, plotted to the right of the data.

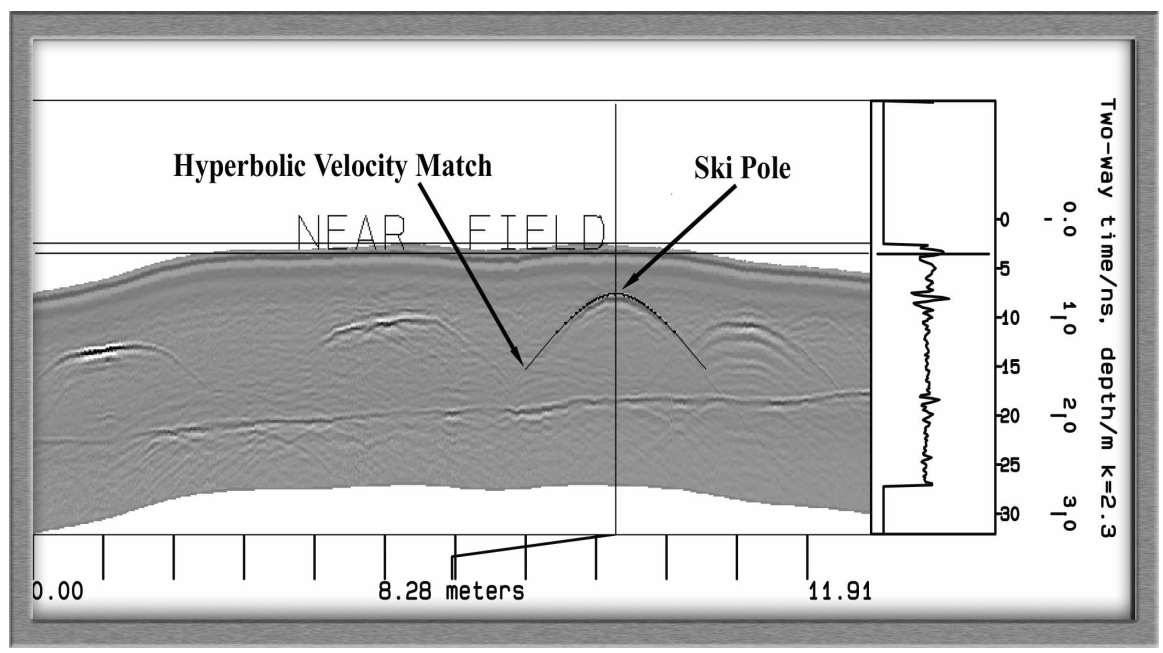


Figure 3.6 Illustrates how the velocity/permittivity was fitted to a hyperbola by matching the GPR reflection from a buried ski pole, using GRORADAR software.

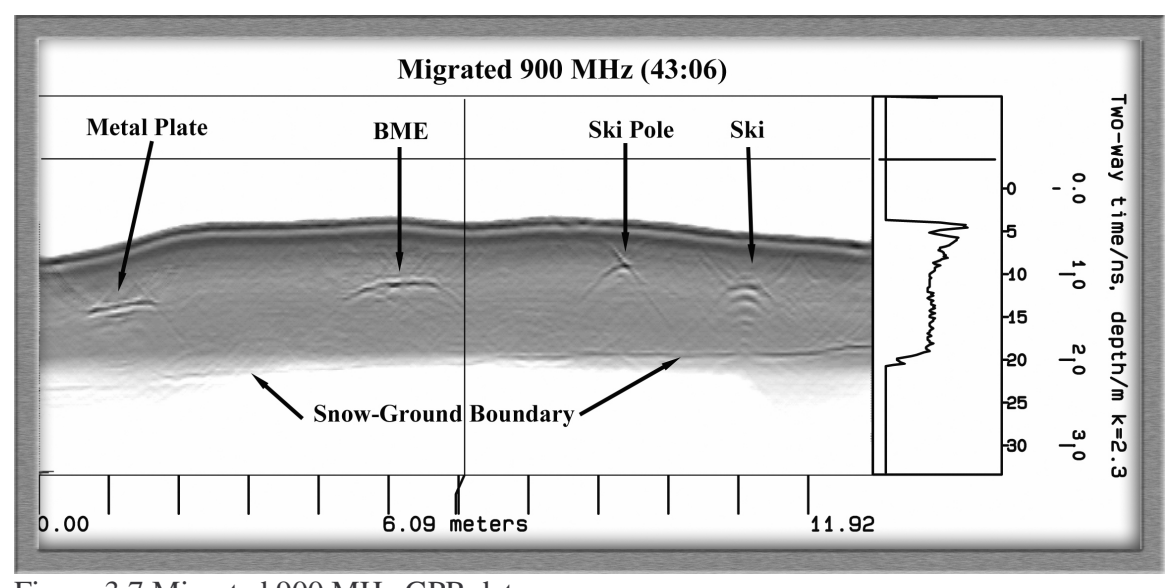


Figure 3.7 Migrated 900 MHz GPR data.

CHAPTER 4

RESULTS

4.1 Temperature Data

Four temperature measurements were recorded during the experiment: the BME's core, the air, the surface snow, and ambient snow. The CorTemp thermometer pill worked well, providing a large amount of data. The BME's core temperature started out at approximately 38° C (close to the human normal 37° C), exponentially declining over 110 hours to 0° C freezing, with the ambient snow temperature at a relatively constant -6° C. Figure 4.1 shows four different temperature measurements for the first 45 hours of the experiment. During the first quarter of the experiment the air temperature dropped below -20° C. It should be noted that the surface snow temperature did reflect the changing air temperature, while the ambient snow temperature at depth did not. The gaps in the data are due to mandatory absence from the experiment site to attend classes.

4.2 GPR Data

All of the raw GPR data files (*.dt1), corresponding header files (*.hd), and survey files (*.edm) are located in Appendix A, along with the field notes.

4.2.1 Visual GPR Data

Appendix B contains the visual cross-section GPR data with the processed and annotated GPR lines of both the 450 MHz and 900 MHz antennas. Some of the

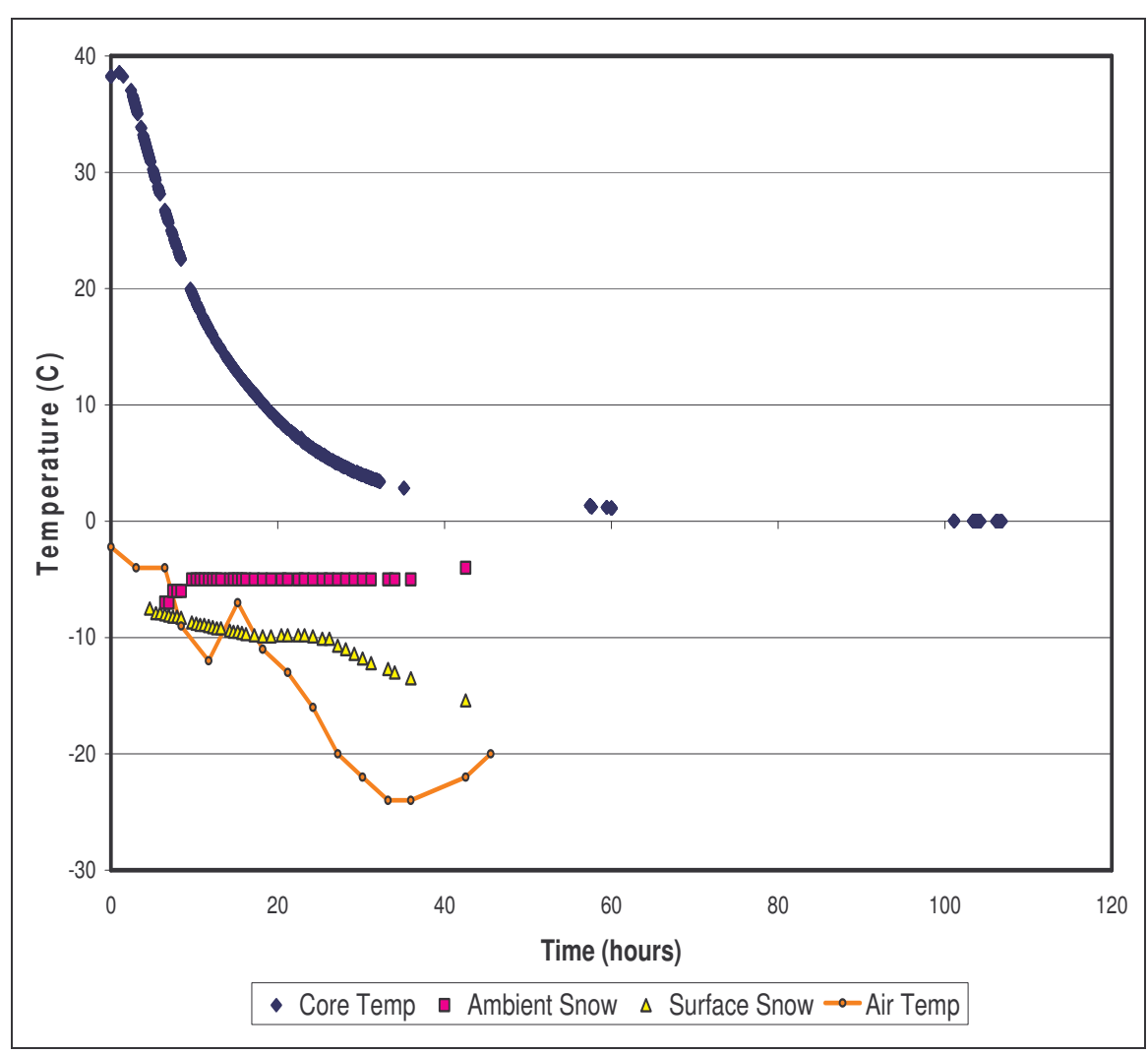


Figure 4.1 Graph providing the temperature data during the survey. Measured data included the core temperature, the ambient snow temperature, the surface snow temperature, and the air temperature.

data comparisons and time-steps have been added to this section for easier reading. GPR lines that are referenced in Figures will contain a label with the frequency and numbers representing the elapsed time since burial in the following format (h:mm). Most Figures containing visual GPR data will contain both frequencies for comparison purposes. Figure 4.2 shows the comparison between the first GPR lines collected using each frequency, at which time the BME's core temperature was at 37°C. In this early phase of the experiment, three targets are easily distinguishable with both frequencies. These targets are the metal plate, the BME, and the snow/ground boundary annotated in Figure 4.2. All three targets are easily mapped with both antennas, which is proof that both frequencies have sufficient penetration and resolution to image the target for this experiment. If you look closely, you can see some reflections (debris) in the 900 MHz that are not visible in the 450 MHz, this is due to the higher resolution of the higher frequency.

The BME's GPR response (across the long axis of the body) is the summation of several reflections from different parts of the body. These main reflectors produced several hyperbolas that merge together in the data. This grouping of reflections and recorded responses could be a unique geometric signature used to detect a body relative to other avalanche debris.

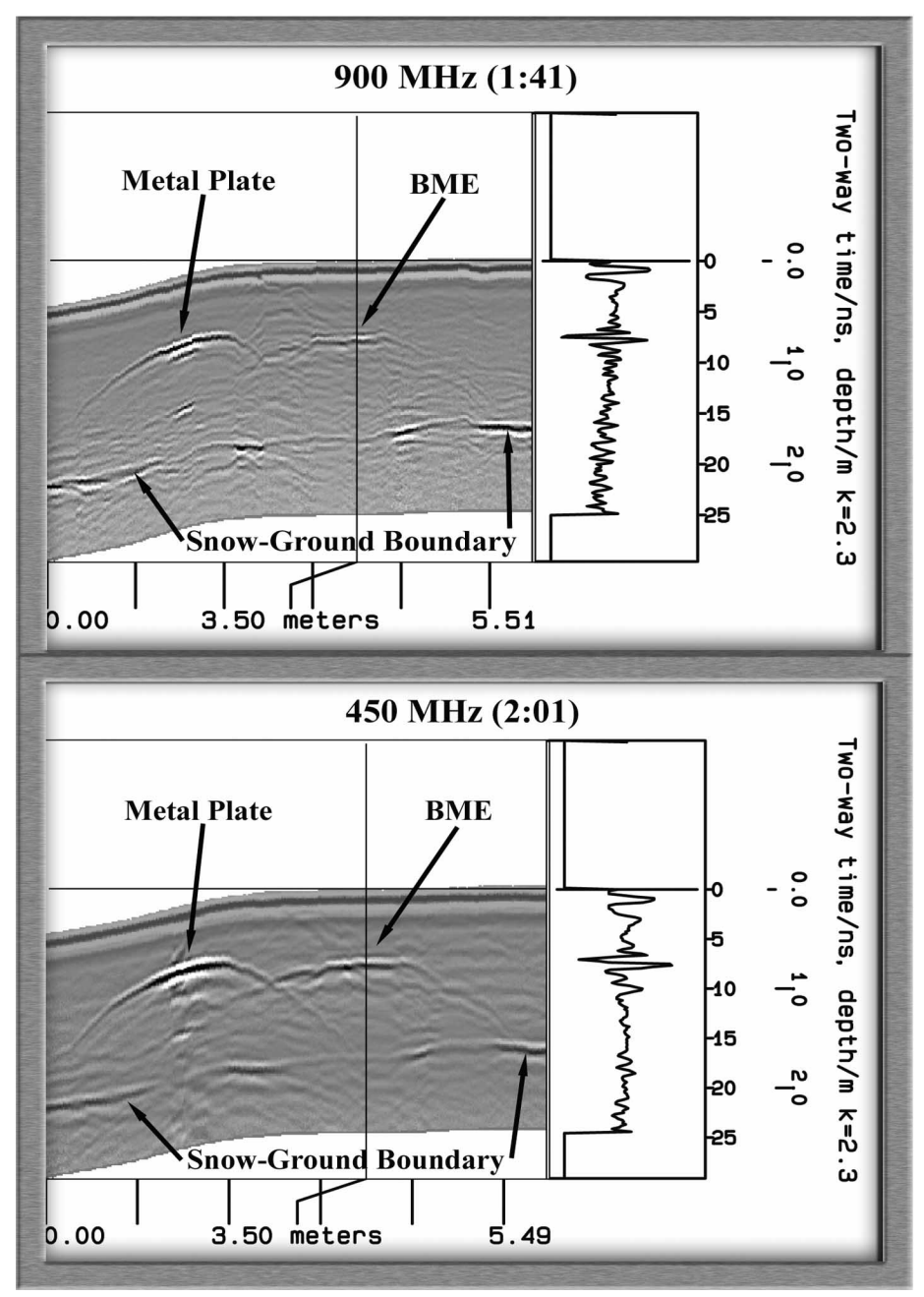


Figure 4.2 900 MHz and 450 MHz earliest recorded data lines for comparison between depth of investigation and resolution. Both frequencies image the metal plate and corresponding diffractions from the edges. Both the BME and the snow-ground boundary are easily recognized. If you look closely, the higher resolution 900 MHz data has some anomalies (small rocks) buried near the surface and located in-between the metal plate and the BME.

Figure 4.3 shows a comparison of data from both antenna frequencies on Line 2. Both GPR measurements were taken at 48 hours after burial, just after the creation of Line 2. In both lines we see one hyperbola, due to the maximum coupling of the GPR traverse perpendicular to the long axis of the BME.

Both Figures 4.2 and 4.3 show that the 900 MHz response provides higher resolution than the 450 MHz. This can be problematic while imaging avalanche debris littered with branches, pine bows, and other debris creating clutter in the data. Figure 4.4 shows a comparison of the last recorded GPR lines, at which time the BME's core temperature was approximately 0° C. The BME is still clearly visible with both frequencies. There is almost no noticeable difference from the BME's GPR response between the earliest and latest GPR recordings, after cooling 36° C. This proves that GPR can effectively image a BME regardless of temperature.

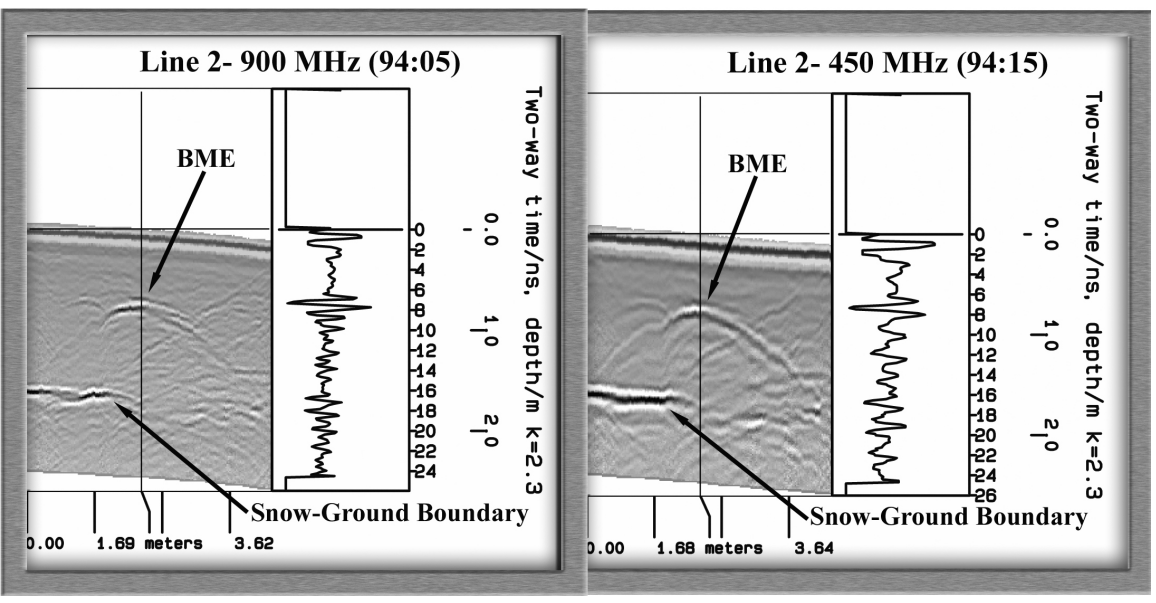


Figure 4.3 Comparison between 450 MHz and 900 MHz GPR data collected along line 2.

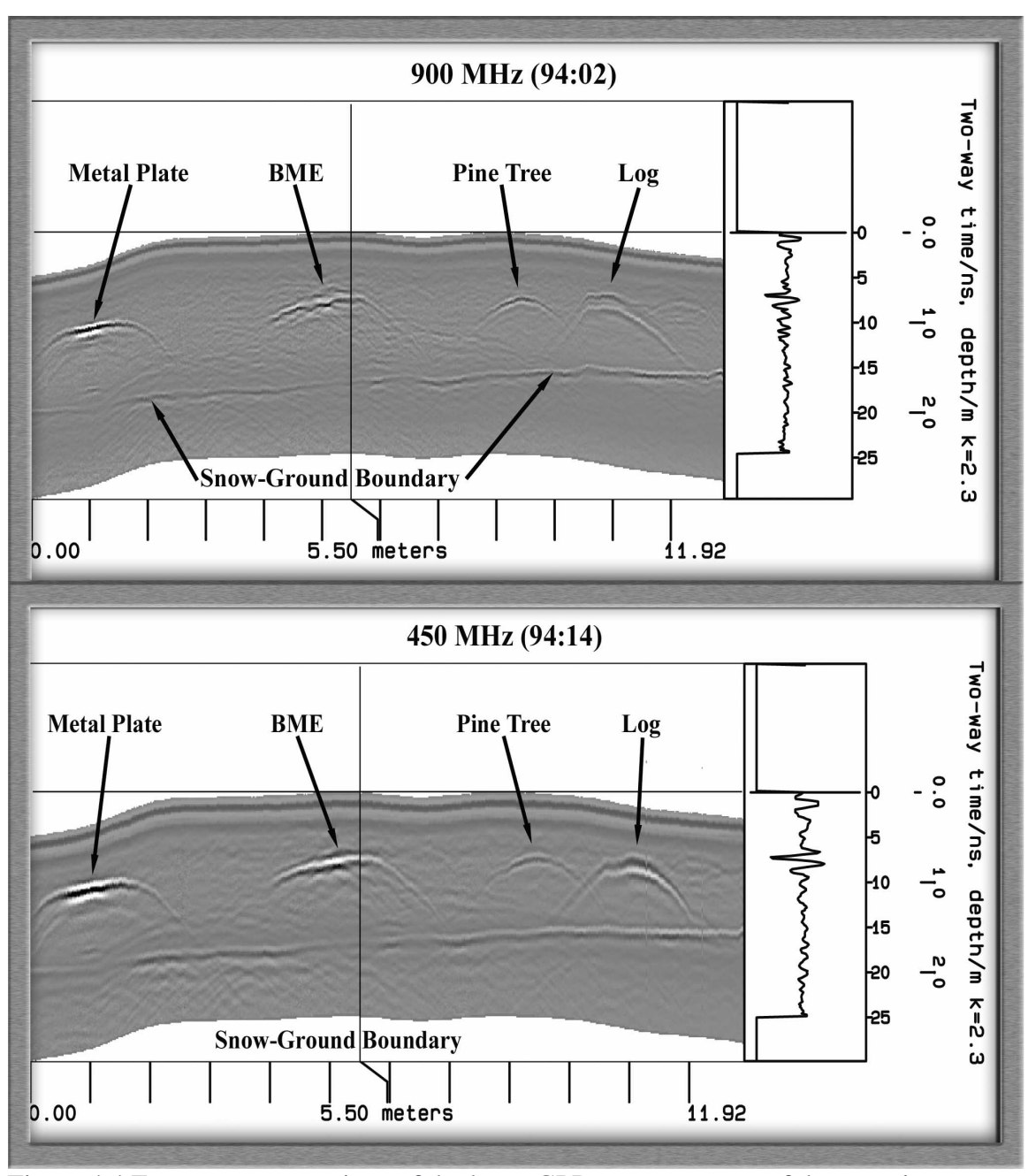


Figure 4.4 Frequency comparison of the latest GPR measurements of the experiment, at which time the BME's core temperature is approximately 0° C. Notice the addition of the pine tree and log near the end of the line.

Figure 4.5 shows two different 450 MHz lines; focus on the natural and manmade objects buried in the test pits near the EOL. The top GPR line has two rocks and two dirt clods buried in the test pits. The bottom GPR line has a ski pole and a ski buried in the test pits. Notice that most of the natural objects look relatively faint, while all the man-made targets and the BME are easily recognizable. The freshly cut log and the pine tree (Figure 4.4) have a similar visual response as that of the BME and the man-made objects. To help gain a better understanding of the data, waveform analysis is performed.

4.2.2 Waveform Analysis

To help provide a more thorough interpretation of the experimental data, waveform analysis was performed. GRORADAR software was used to pick the normal incident trace of a GPR reflection for the various targets, which was output as a binary file. Matlab software was used to help analyze, interpret, and display the different traces. Figure 4.6 shows the trace of a normal incident 900 MHz GPR reflection from the BME. This is one example of what the traces look like. In Figure 4.6 the correct zero time has been set at the first energy or direct air wave arrival. For future reference, when discussing the waveform shape and amplitude, just the target waveform will be shown (as indicated with red). All the full length traces for each target can be found in Appendix C.

All of the trace amplitudes were normalized to the largest value, the direct arrival, displaying the measurement as "relative amplitude". This was to help account for instrument drift during the experiment that might have occurred due to an extended period of use (96 hours), changing air temperature, and other weather conditions.

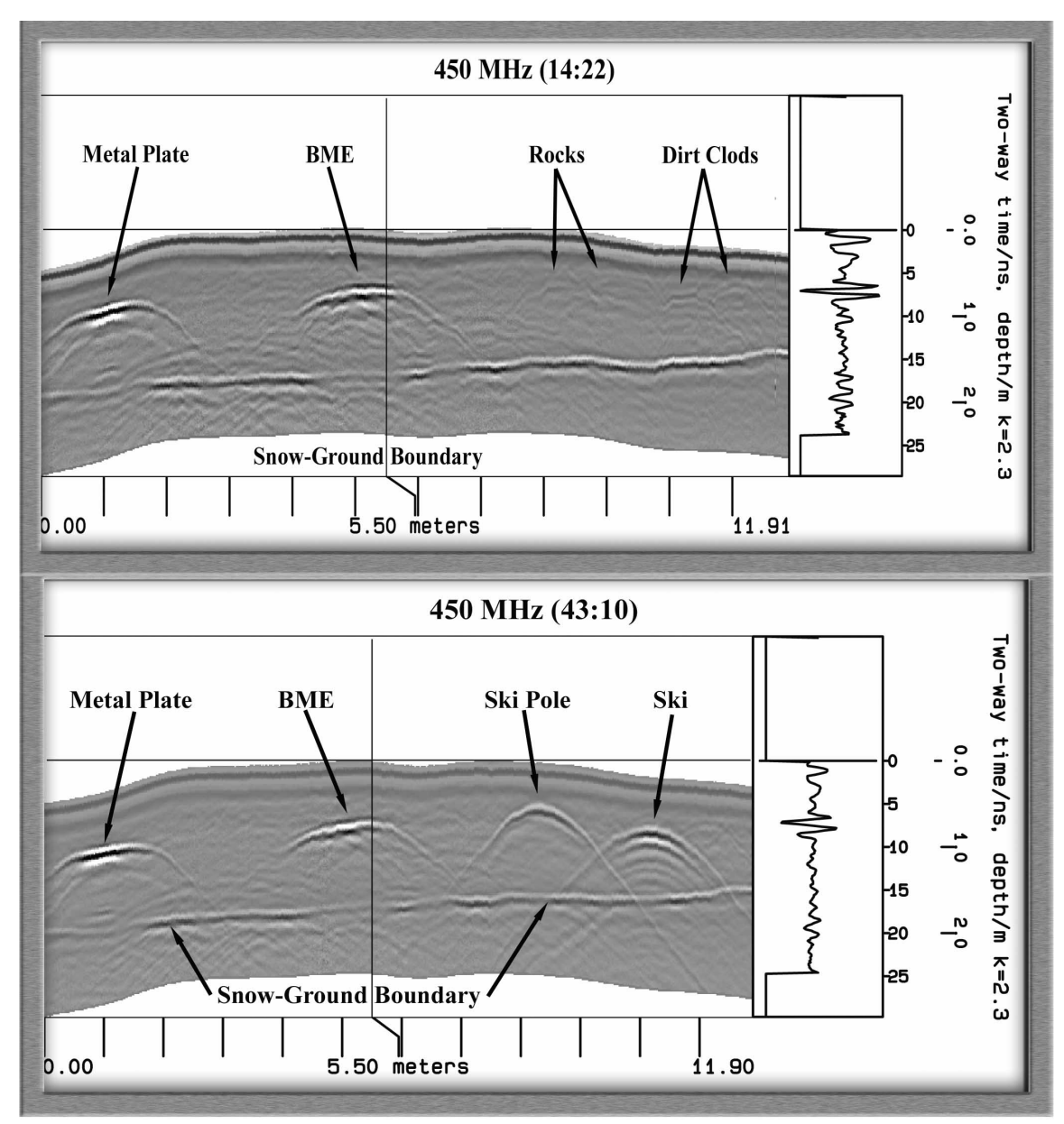


Figure 4.5 450 MHz GPR response of natural (rocks and dirt clods) and man-made objects (ski pole and ski).

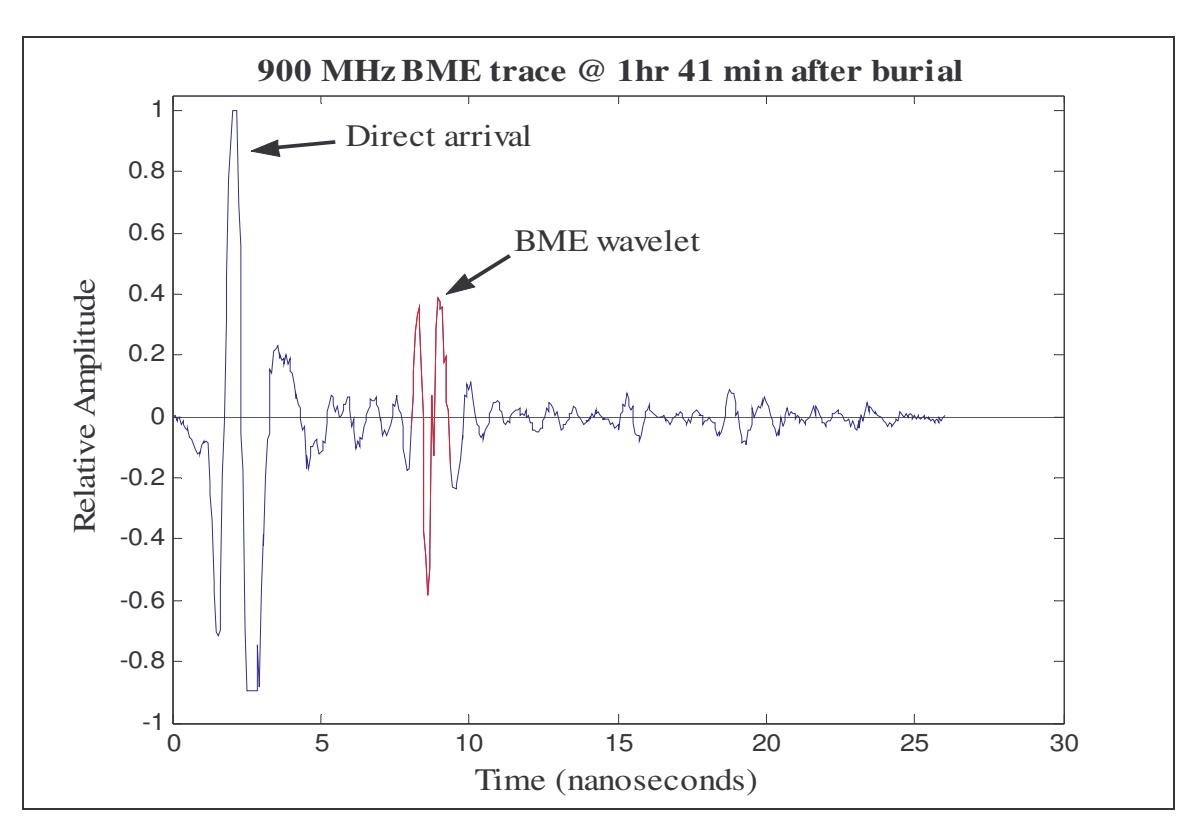


Figure 4.6 Depicts a normal incident GPR reflection trace from the BME. The BME waveform is shown in red and the direct arrival is annotated. The y-axis has been normalized to the largest value, the direct arrival.

Figures 4.7 and 4.8 show several 900 MHz and 450 MHz target waveforms, respectively, that have been picked out of each trace for easier reading. The targets include three different BME waveforms, natural, and man-made objects. In the bottom right corner of each waveform graph there is a fractional number. This represents the amount of relative reflected energy from the target, where the metal plate is a perfect reflector. The early BME reflection has the largest relative amplitude (excluding the metal plate). As the BME froze, the amplitude did decrease as represented by the later time BME waveforms. The snow / ground boundary has the next largest relative amplitude (0.39). This large reflector is helpful because it sets a distinguishable boundary to aid in the interpretation process. The later BME waveforms amplitudes are relatively similar to the man-made objects with metal like the ski, ski pole, and ski boot (0.36-0.29). The smallest reflections were from the natural objects and the plastic helmet (0.26-0.12). Notice the wood and rock amplitudes are smaller than all of the BME's amplitudes. There are many similarities between both frequencies, all of this is true of both. It should be noted that there was no 450 MHz measurement of the helmet.

The next observation from Figures 4.7 and 4.8 is that the BME waveform has a unique shape relative to all the other target waveforms. The metal plate emphasizes the "typical" waveform with two negative peaks and only one positive peak. Where as, the BME has a "unique" waveform that has two positive peaks and one negative peak. The reason for this unique shape will be explained in the modeling chapter.

Figure 4.9 has nine 450 MHz BME waveforms taken during different times, ranging from 2 hours to 94 hours after burial. There are three main observations as to how the waveform evolves with the drop in core temperature. In the first two graphs, the first positive peak is smaller than the second positive peak. In all the other graphs they are of similar size. Secondly, the amplitude starts out increasing rapidly. At about 8 hours after burial, the waveform reaches a maximum and then slowly decreases (this point is emphasized with Figure 4.10). The earliest and latest measurements have approximately

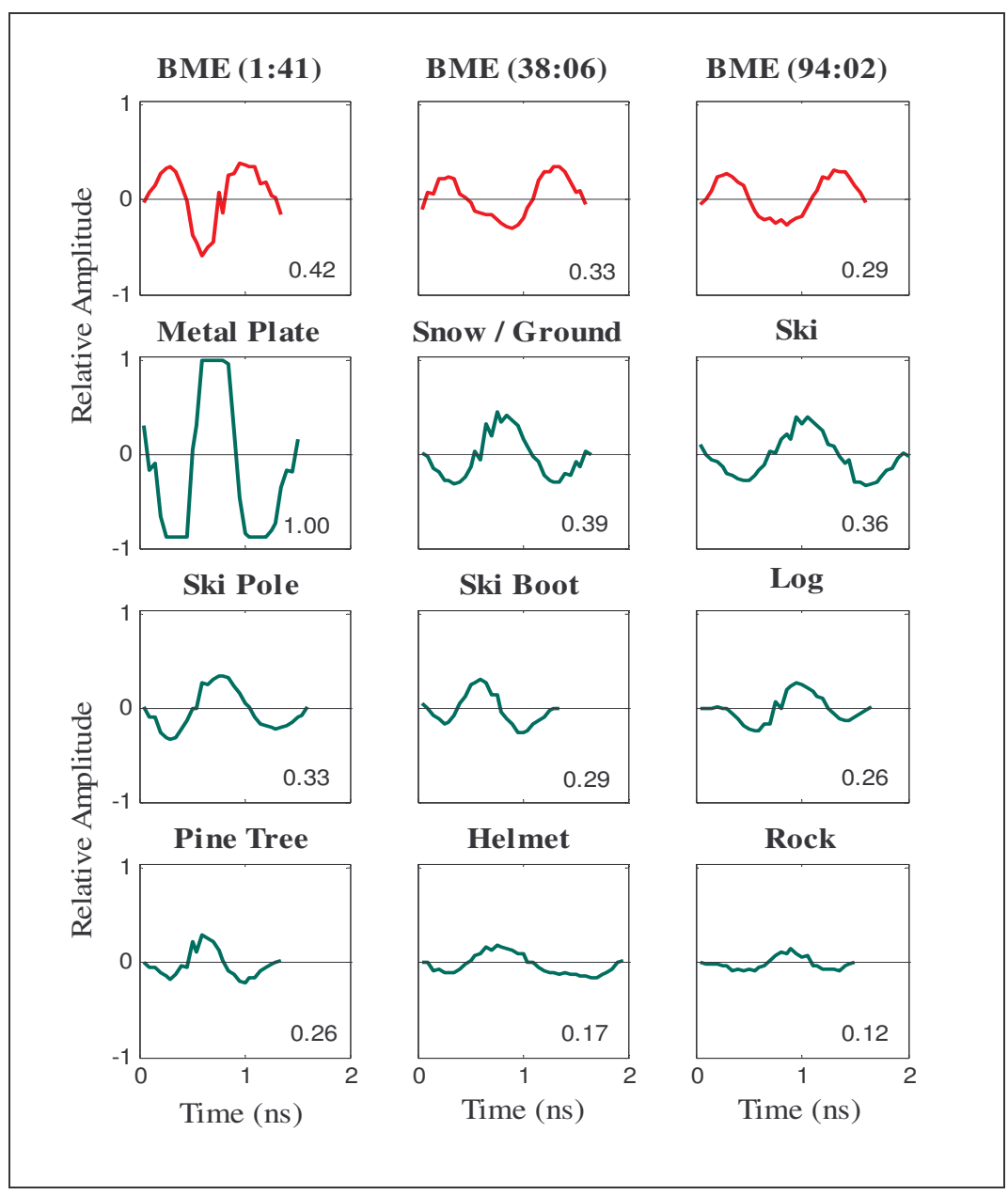


Figure 4.7 Depicts several different 900 MHz GPR reflection waveforms from the BME, natural, and man-made objects. The fractional amount of reflected energy (relative to the direct arrival) is located in the lower right corner.

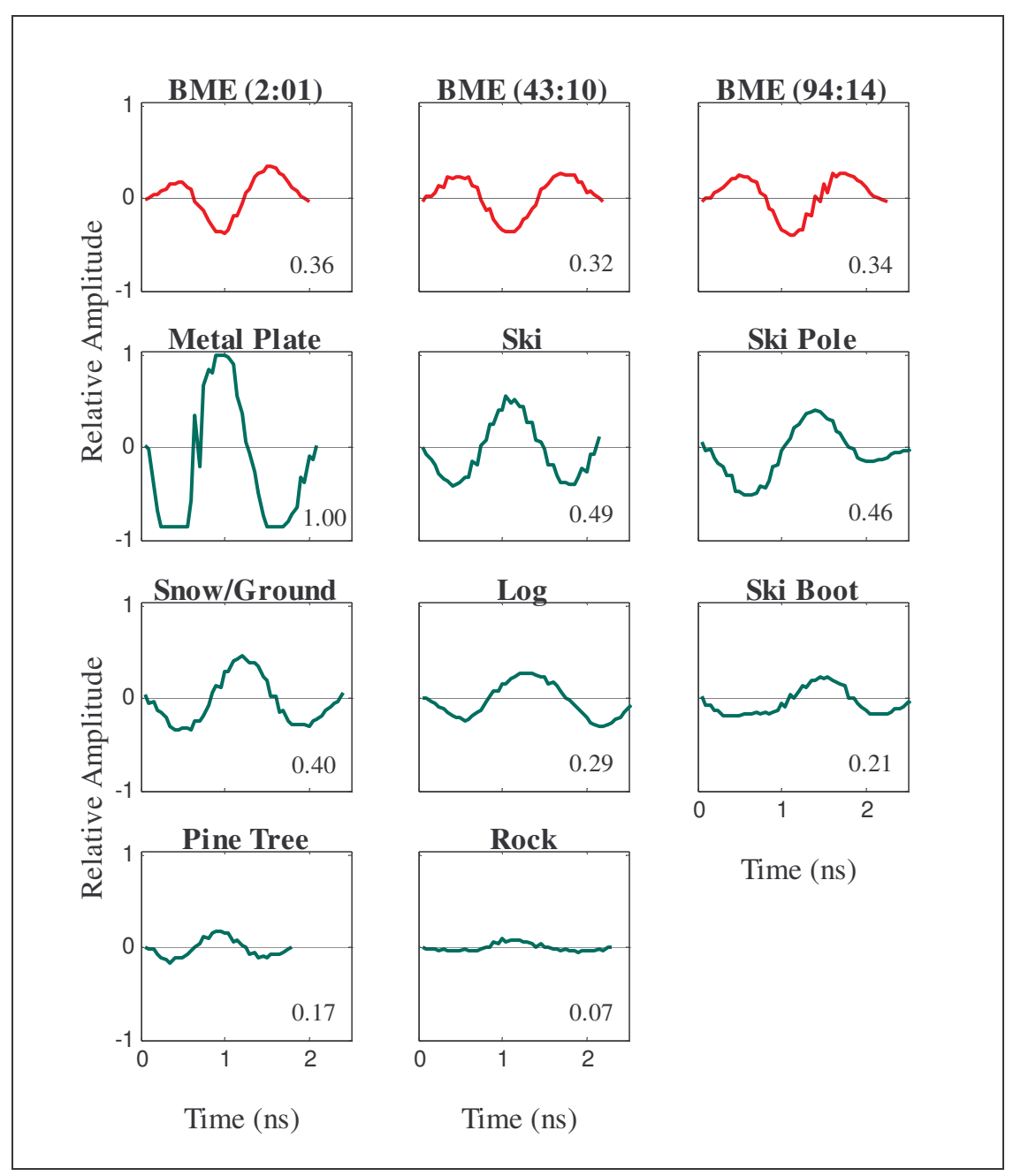


Figure 4.8 Depicts several different 450 MHz GPR reflection waveforms from the BME, natural, and man-made objects. The fractional amount of reflected energy (relative to the direct arrival) is located in the lower right corner. Notice that there is no measurement for the helmet.

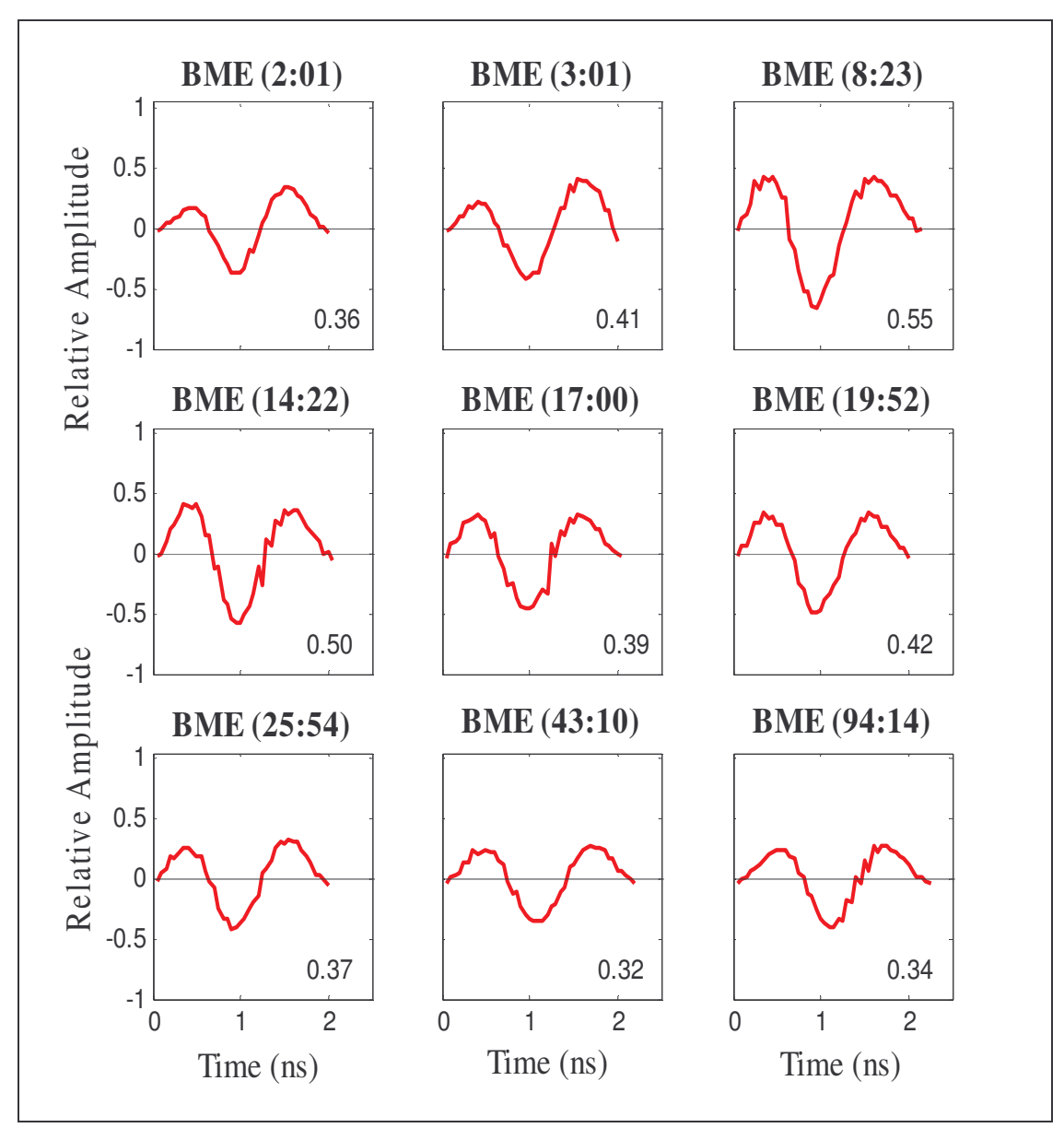


Figure 4.9 450 MHz GPR BME waveforms taken from different times throughout the experiment. The fractional amount of reflected energy (relative to the direct arrival) is located in the lower right corner.

the same relative amplitude. Third, the waveform spreads out horizontally (in time), or broadens as the core temperature dropped.

Figure 4.10 provides quantitative information for the 900 MHz BME waveforms maxima and minima during the experiment. As seen in Figure 4.9, there are two maximum peaks and one minimum peak associated with the BME's waveform. This Figure illustrates how the waveform evolved with temperature. The peaks start out increasing at a rapid rate, where at about 8 hours after burial an exponential decline occurs. The exponential decline is best portrayed in the minimum peak data.

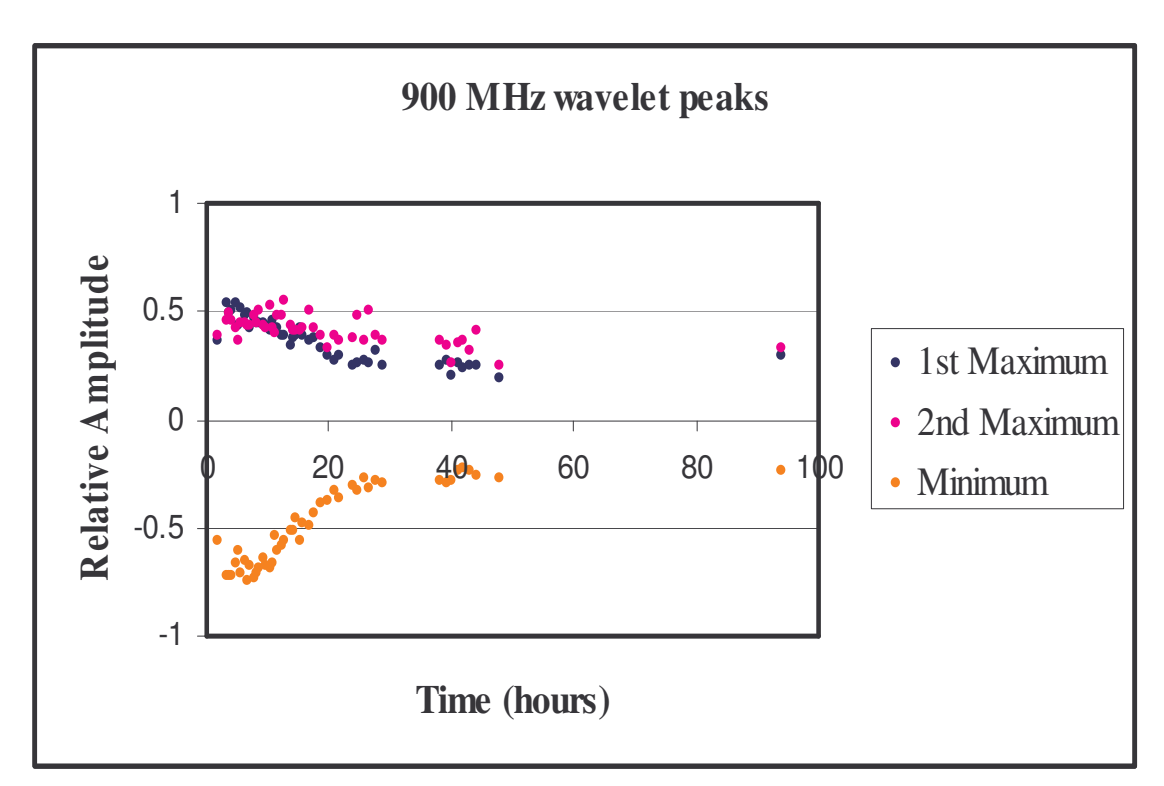


Figure 4.10 900 MHz BME waveform amplitudes versus time.

The minimum appears to level out at approximately 40 hours after burial. At this time, the BME has lost approximately 92% of its core temperature, relative from 38° to 0° C. This shows a direct correlation between the core temperature and the amount of reflected energy.

4.2.3 Frequency Analysis

The waveforms for each target were analyzed for frequency content. Matlab software was used to change the time-series waveform into frequency by using a 64 point FFT. The waveforms typically had between 30 and 50 points. The waveforms were trimmed down so that the first and last value used were the last points before crossing the 0 x-axis. Figure 4.11 shows five different methods for padding a 450 MHz BME (2:01) waveform. The Hanning window (Hann filter) method was determined to be the best and is the method used for all other data (McClellan et al., 1999).

Figures 4.12 and 4.13 display the frequency response for the 450 MHz and 900 MHz (respectively) for five different BME reflections during the survey. We see that the amplitude is consistent, while as the experiment progressed, both frequencies show a shift to a lower frequency response.

Figures 4.14 and 4.15 display the frequency response for both 450 MHz and 900 MHz (respectively) for several different target reflections. Here, there is a lack of any correlation between frequencies. With the 900 MHz data, the large amplitudes of the wood are reduced in the power spectrum, while with the 450 MHz data, the log has a much larger (almost double) power spectrum.

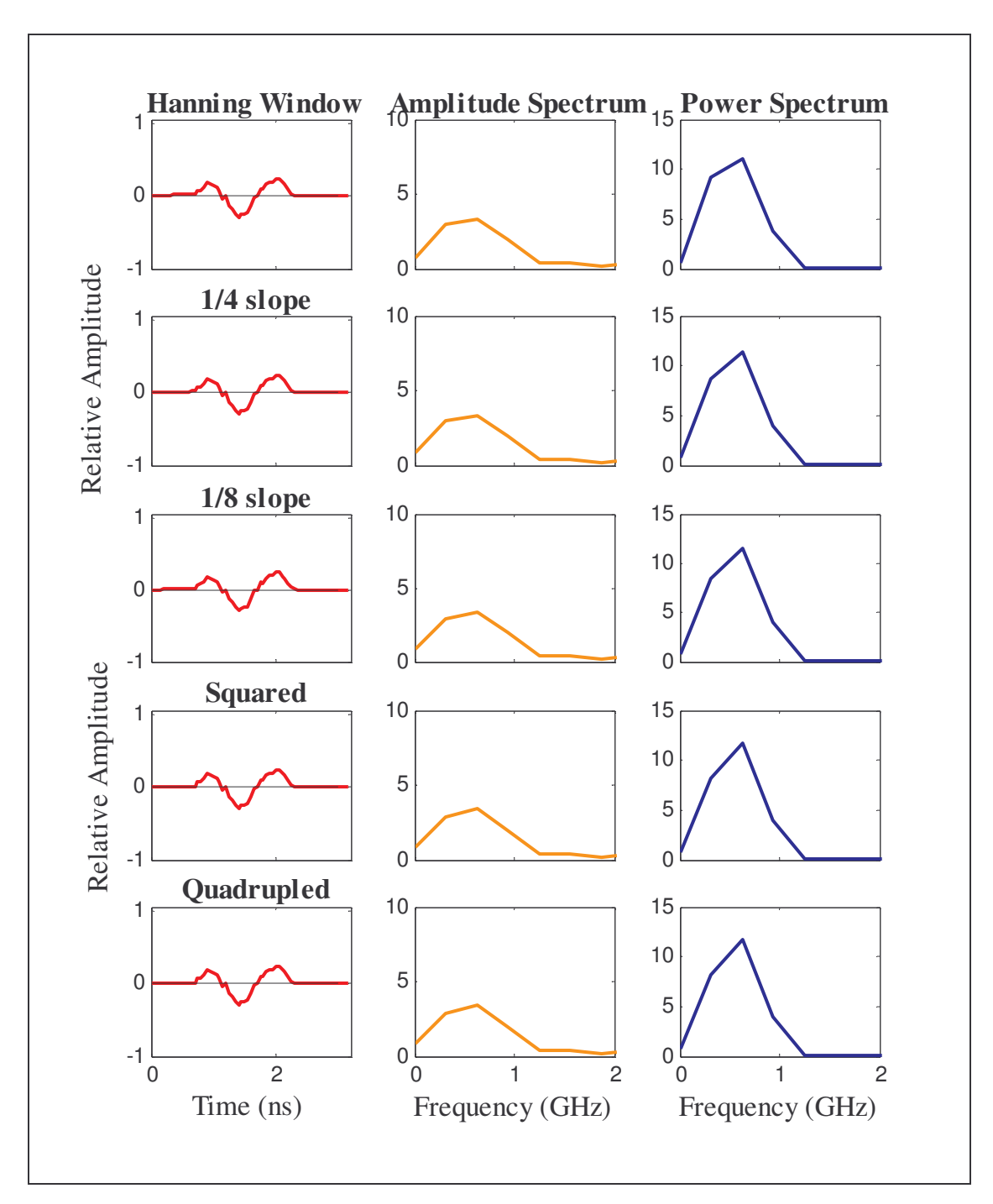


Figure 4.11 Several different methods to pad the waveforms before applying the 64 point FFT; eventually the Hanning Window was applied for FFT investigations (McClellan, 1999).

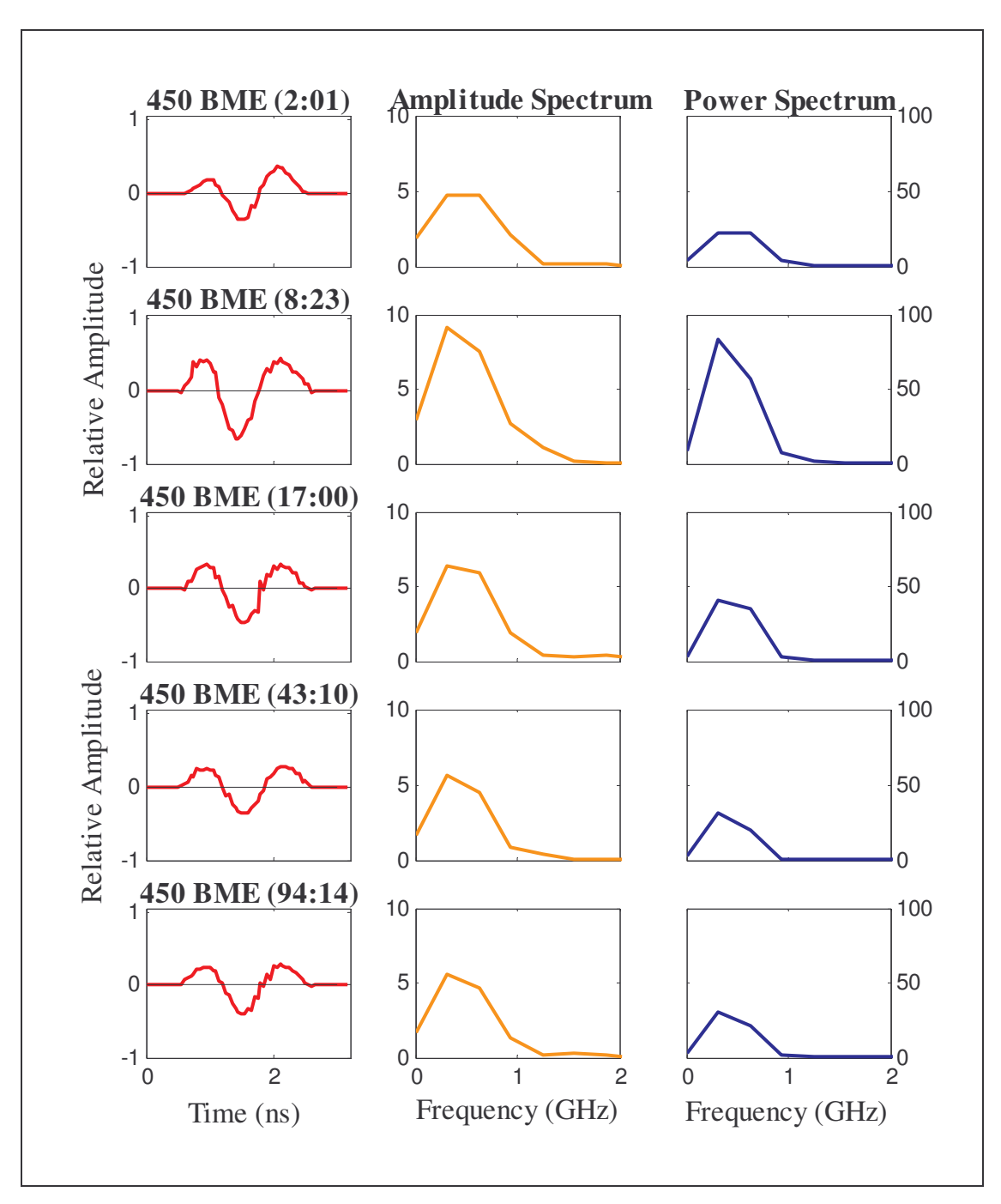


Figure 4.12 FFT of 450 MHz BME reflections at different time during the experiment.

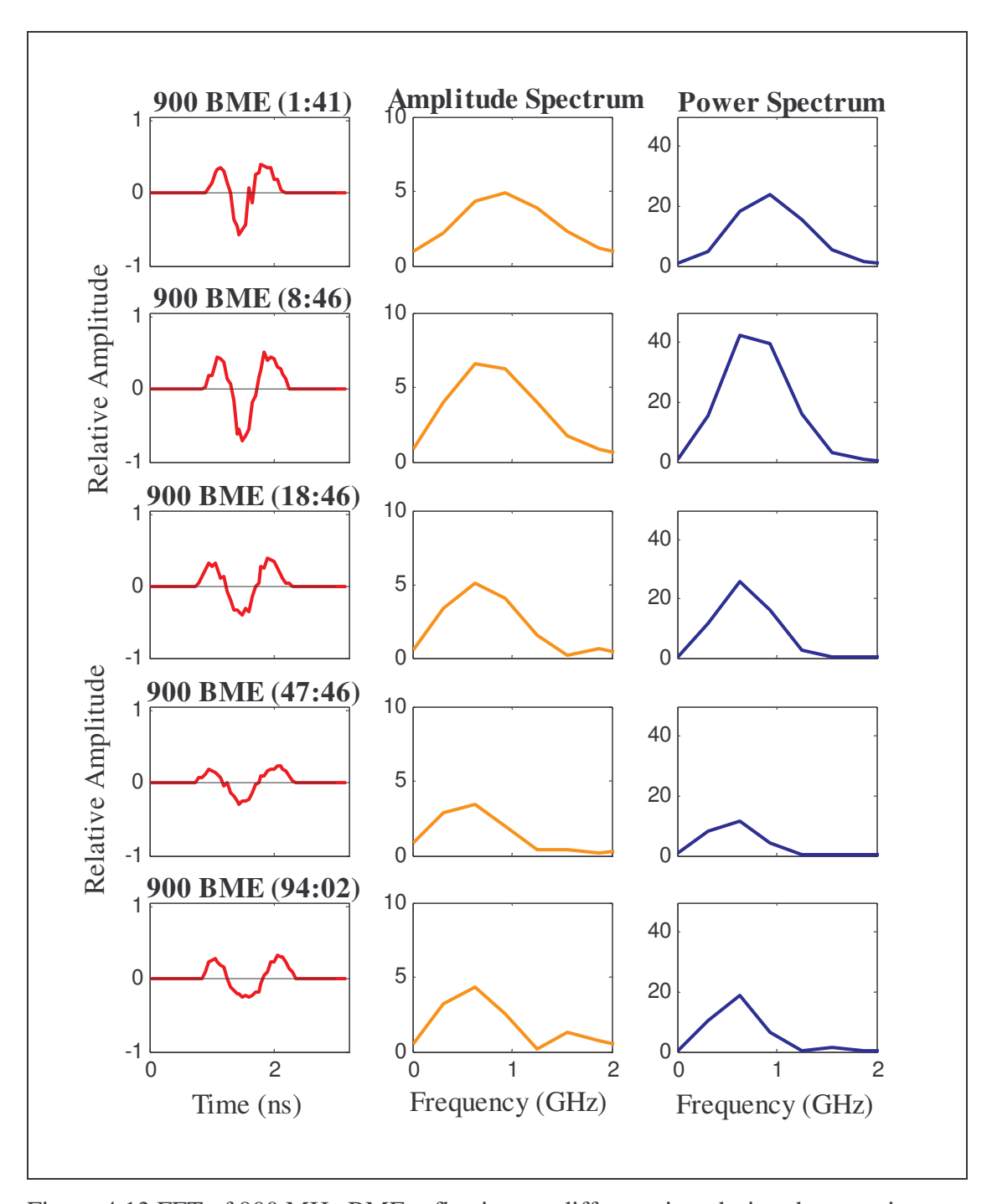


Figure 4.13 FFT of 900 MHz BME reflections at different time during the experiment.

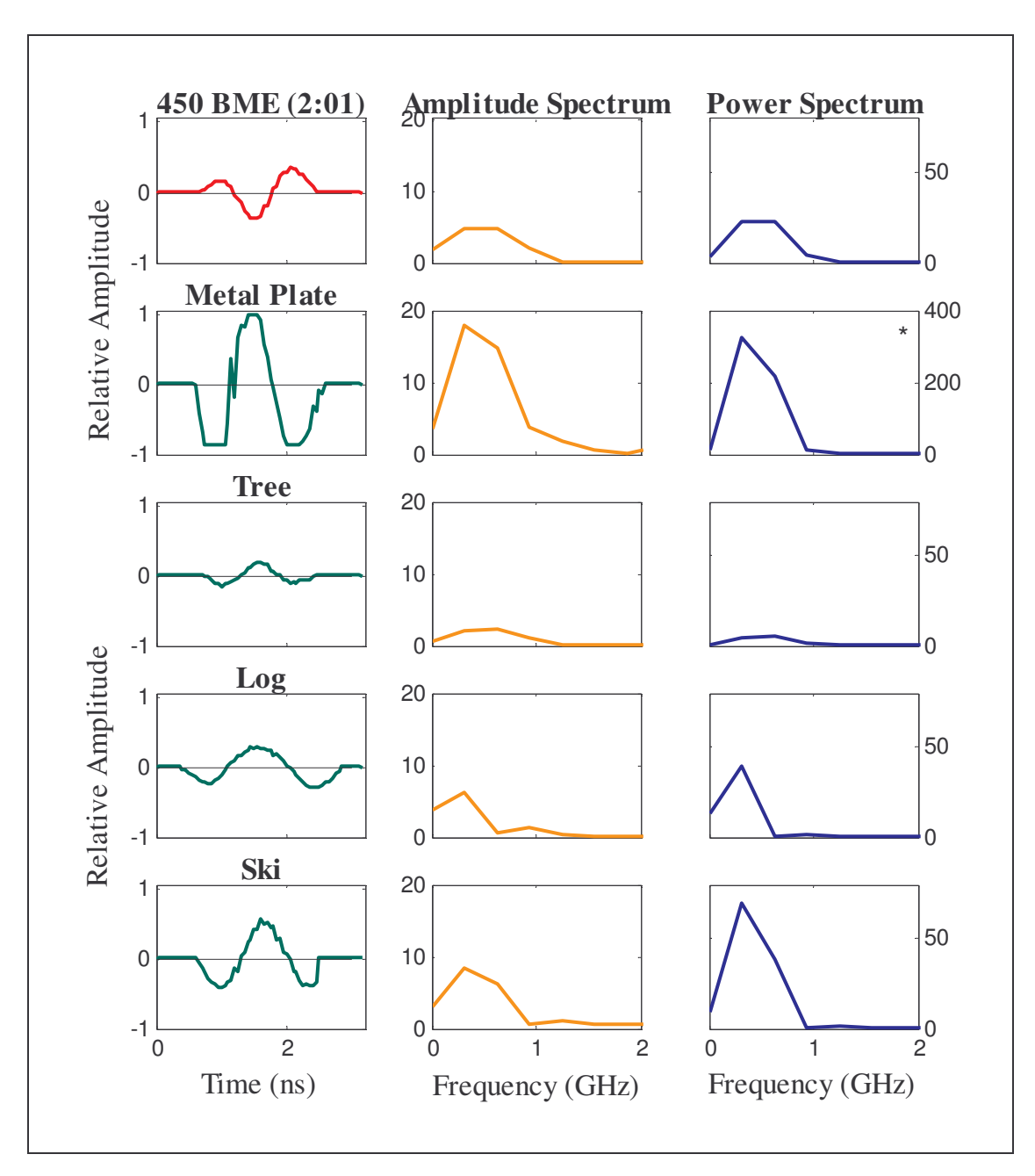


Figure 4.14 FFT of different 450 MHz target reflections. *Notice that the metal plate has a different scale for the power spectrum.

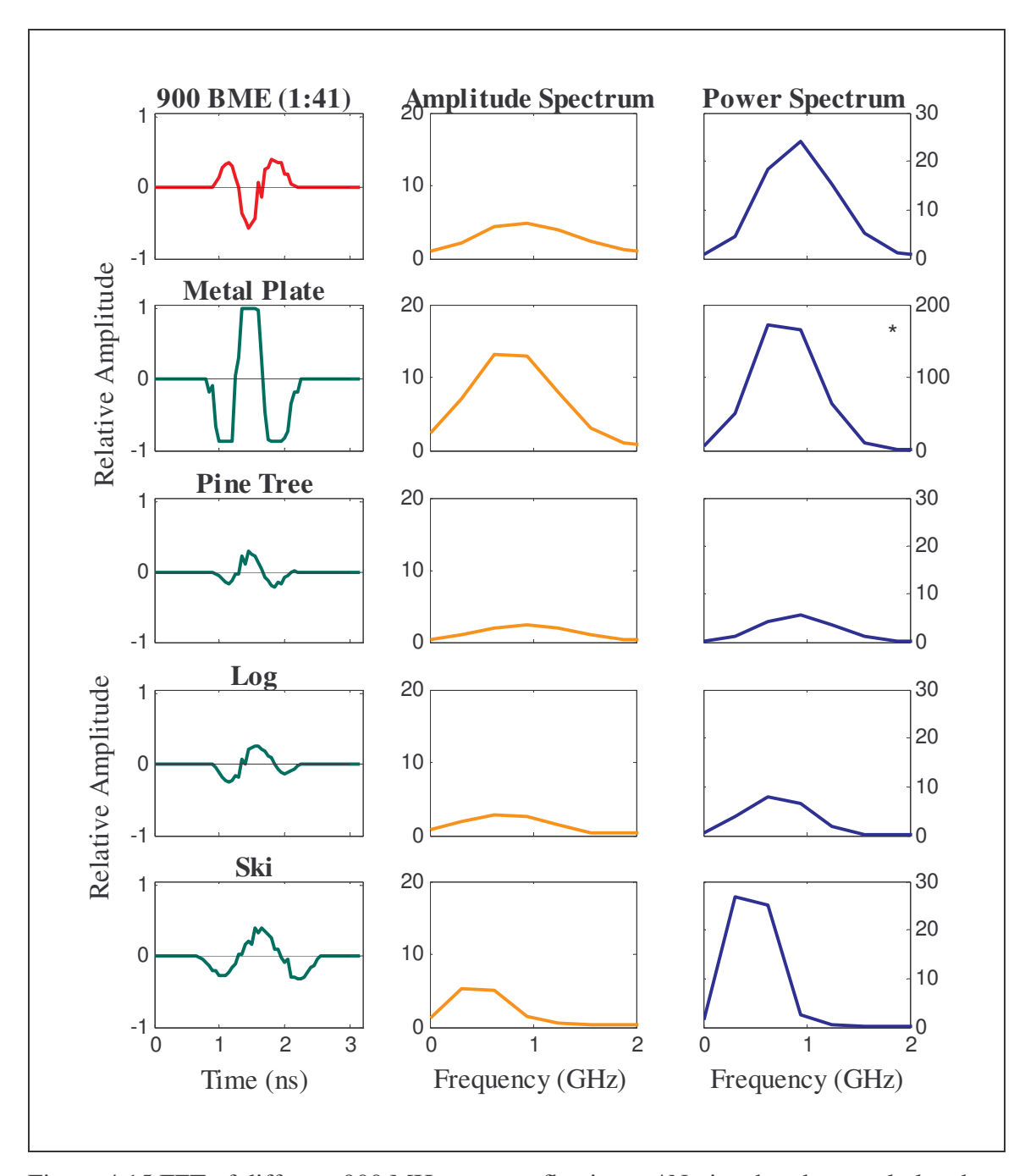


Figure 4.15 FFT of different 900 MHz target reflections. *Notice that the metal plate has a different scale for the power spectrum.

4.3 Error Analysis

Sources of error exist in all experiments, including this one. With any GPR survey, there is always a question as to the accuracy of the depth measurement. Measuring the depth of a subsurface target with GPR can have several sources of error. These sources of error include: picking the wrong zero time, incorrect determination of the dielectric permittivity (produces incorrect velocity), and even variances in the central bandwidth of the antenna. During the experiment, the surface snow temperature ranged from -7° C to -15° C. Because the dielectric permittivity of snow varies depending on temperature, the surface snow temperature would have slight changes of its dielectric permittivity. It is unknown how deep this temperature change penetrated into the snow pack. However, in the recorded temperature ranges, little variation in dielectric permittivity is observed.

One of the biggest sources of error, for any geophysical experiment, is in determining the location of the measurement. Fiducial markers were used in this experiment to help reduce this error. The location error becomes a problem when comparing the BME reflections over time. Picking the same BME trace from each GPR line proved to be difficult. It should be noted that the actual BME reflection was composed of approximately 80 traces, which helped the picking process.

Error is also associated with the amplitude analysis that was performed. There can be several sources of background noise in all GPR data due to several types of radio-frequency interference (cell phones, portable radios, etc.). It is then important to determine the amount of background error in the amplitude analysis. This was performed by looking at information in the traces before the transmitter is fired. Figure 4.16 shows the first 10 nanoseconds of a raw data trace, emphasizing the background noise. This noise amounts to a \pm 5% error in all of the reflected amplitude fractions. To help

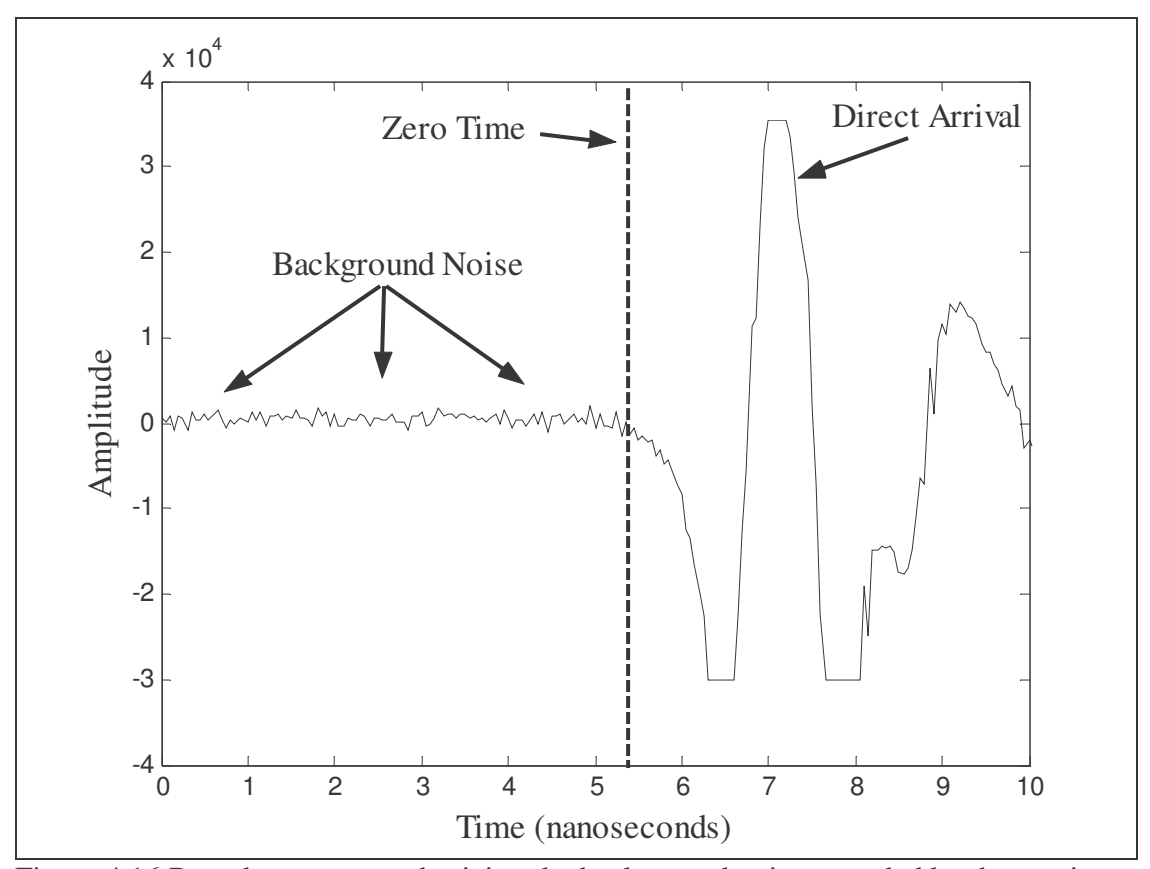


Figure 4.16 Raw data trace emphasizing the background noise recorded by the receiver prior to the transmitter energy.

account for instrument drift, all of the amplitudes measured were normalized by the amplitude of the direct arrival located within the same trace.

CHAPTER 5

MODELING

5.1 Full Waveform Model

Full waveform modeling was performed using the GRORADAR software (version 2003.11). This is a convolution model that uses medium properties to physically model the behavior of an EM pulse traveling through different layers. This model demonstrates how the physical properties of each layer alter the signature of a radar scan. Some assumptions of the model are: the EM wave is in the far field, and the layers are flat, horizontal, homogeneous, isotropic, non-magnetic, as well as volumes and surfaces interfaces are smooth relative to a wavelength (Duke, 1990). Figure 5.1 is a picture of the layered model used, with different input parameters (thickness (m), relative dielectric permittivity (ε_r), conductivity (σ (mS/m)), and the EM wavelength (λ (cm)) associated with each medium. Figure 5.3 shows the 900 MHz modeled response for five different scenarios. The first (left to right), shows the response from three layers, snow, a human body, and snow. The final four models have three new layers (ice, air, and frozen skin) that are located between the snow and human body. The final layered model is: snow, ice, air, frozen skin, unfrozen human body, and snow. The final four models vary only with the thickness of the three new layers. Each layer was given a 1cm increment. So, in the final model each new layer has a thickness of 4 cm. In this case, the thin layers provided constructive and destructive interference completely changing the shape of the waveform. Notice how the waveform starts out "typical" and then eventually evolves into a "unique" shape. The final model is a similar match to the shape of the observed BME's reflected waveform.

Figure 5.4 is the 450 MHz modeled response for the same layered model. With the lower resolution, the layer thickness needs to be 6 cm before the waveform shape can make the full transition from "typical" to "unique". Both models and measured data did agree with each other that a 4 cm air pocket had developed after 2 hours of burial for this BME experiment.

5.2 Sensitivity Analysis

The model was then tested for the sensitivity of each input parameter (thickness, conductivity, and dielectric permittivity). For this model, the sensitivity refers to changes in the waveform shape from a distinguishable "unique" shape. For example look at Figure 5.3, where at X = 1 the waveform shape is not "unique" and at X = 2 the waveform shape is in the beginning stages of the "unique" shape.

The parameter that had the least impact on the model was the conductivity. The conductivity value of the frozen skin and body layers was decreased to 0 (mS/m) with little consequence to the waveform shape. The dielectric permittivity values were the next most sensitive model parameter. The most sensitive permittivity layers were the snow, ice, and air layers. With these three layers the model was sensitive to a change of \pm 1.5 (relative dielectric permittivity). With the other permittivity layers, the model was sensitive to a change of \pm 20 (relative dielectric permittivity). By far, the layer thickness (of the thin layer sequence) was the most sensitive model parameter and varied with frequency. For the 450 MHz and 900 MHz models, the three layer thicknesses were sensitive to \pm 1 cm and \pm 0.5 cm respectively, as can be seen in Figures 5.3 and 5.4.

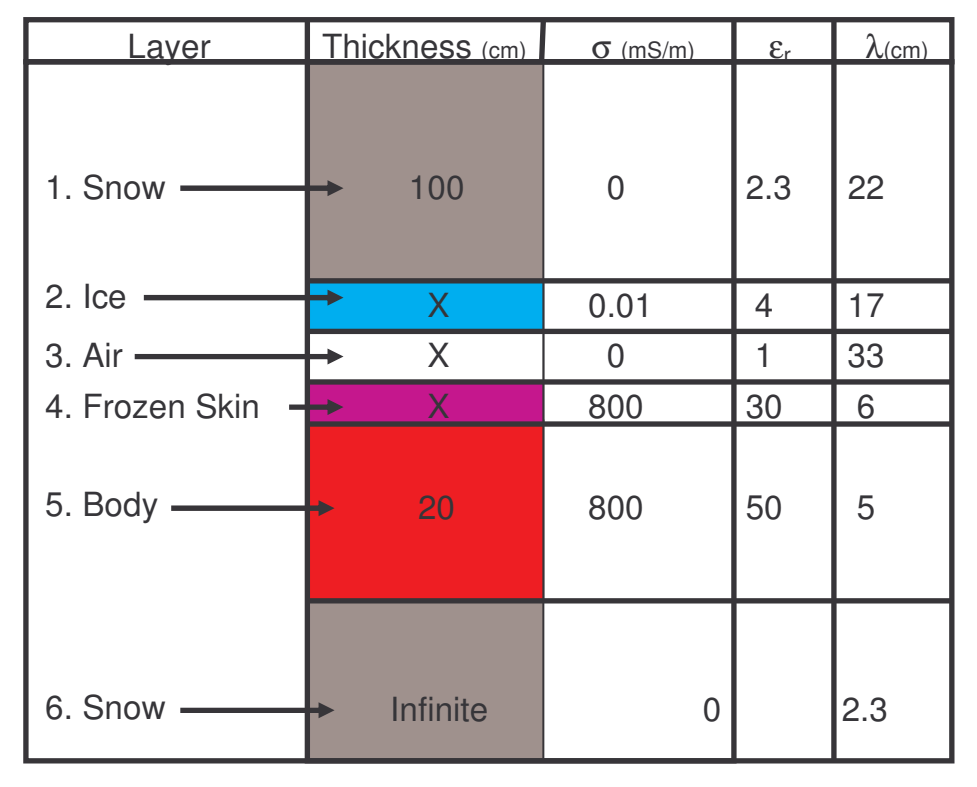


Figure 5.1 Picture of the layer sequence used for the models in Figure 5.3 and 5.4.

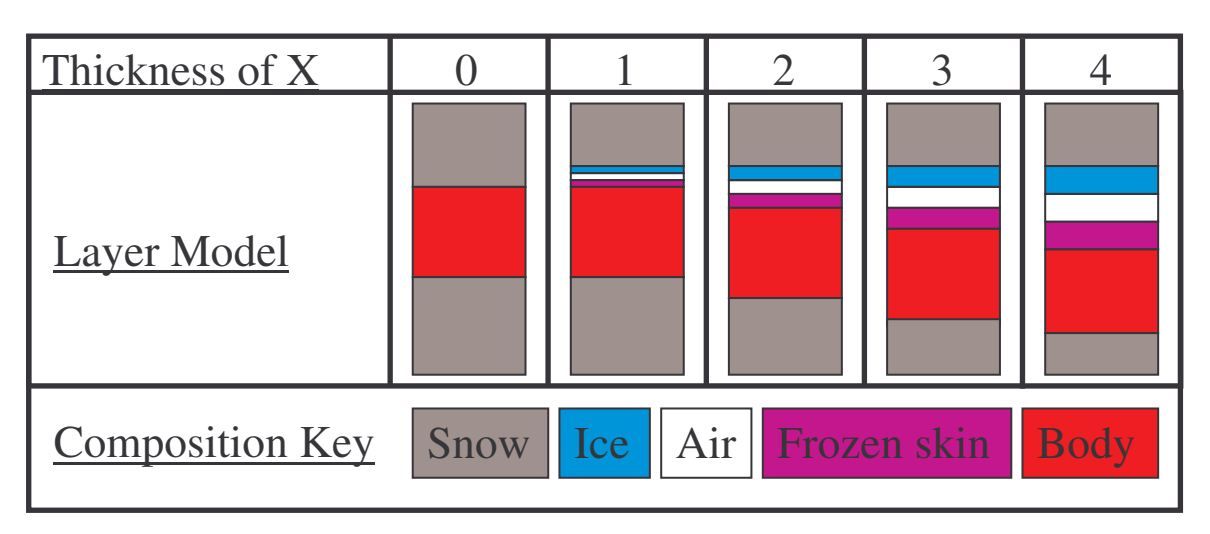


Figure 5.2 Graphic display of how the value of X affected the layered models in Figures 5.3 and 5.4.

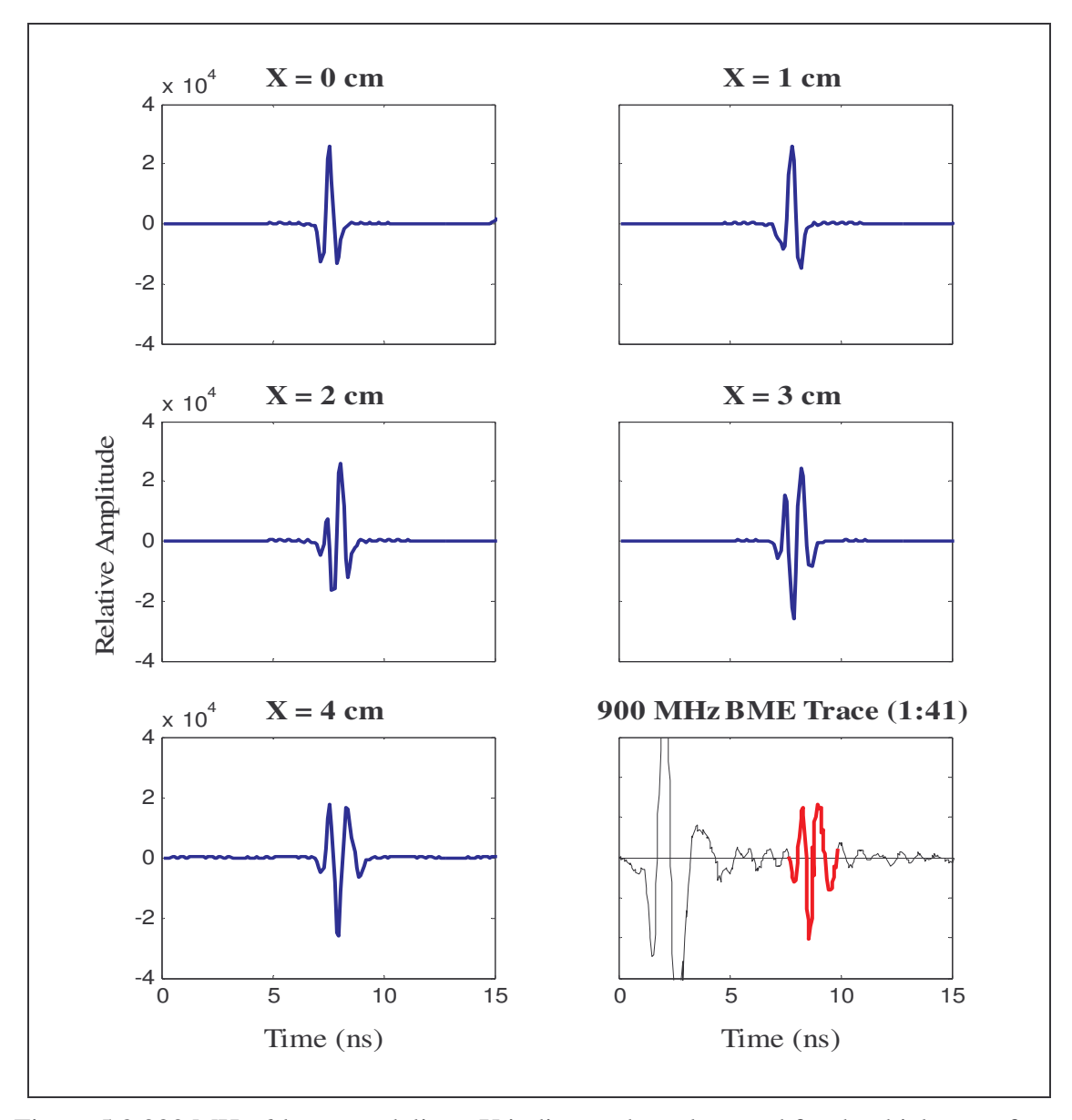


Figure 5.3 900 MHz 6 layer modeling. X indicates the value used for the thickness of layers 2, 3, and 4 (ice, air, frozen skin). Notice the evolution of the waveform shape as constructive and destructive interference develops. The last box in the lower right shows the measured BME reflection (red) at 1 hour and 41 minutes after burial. Notice how this matches well with the X = 4 model shape.

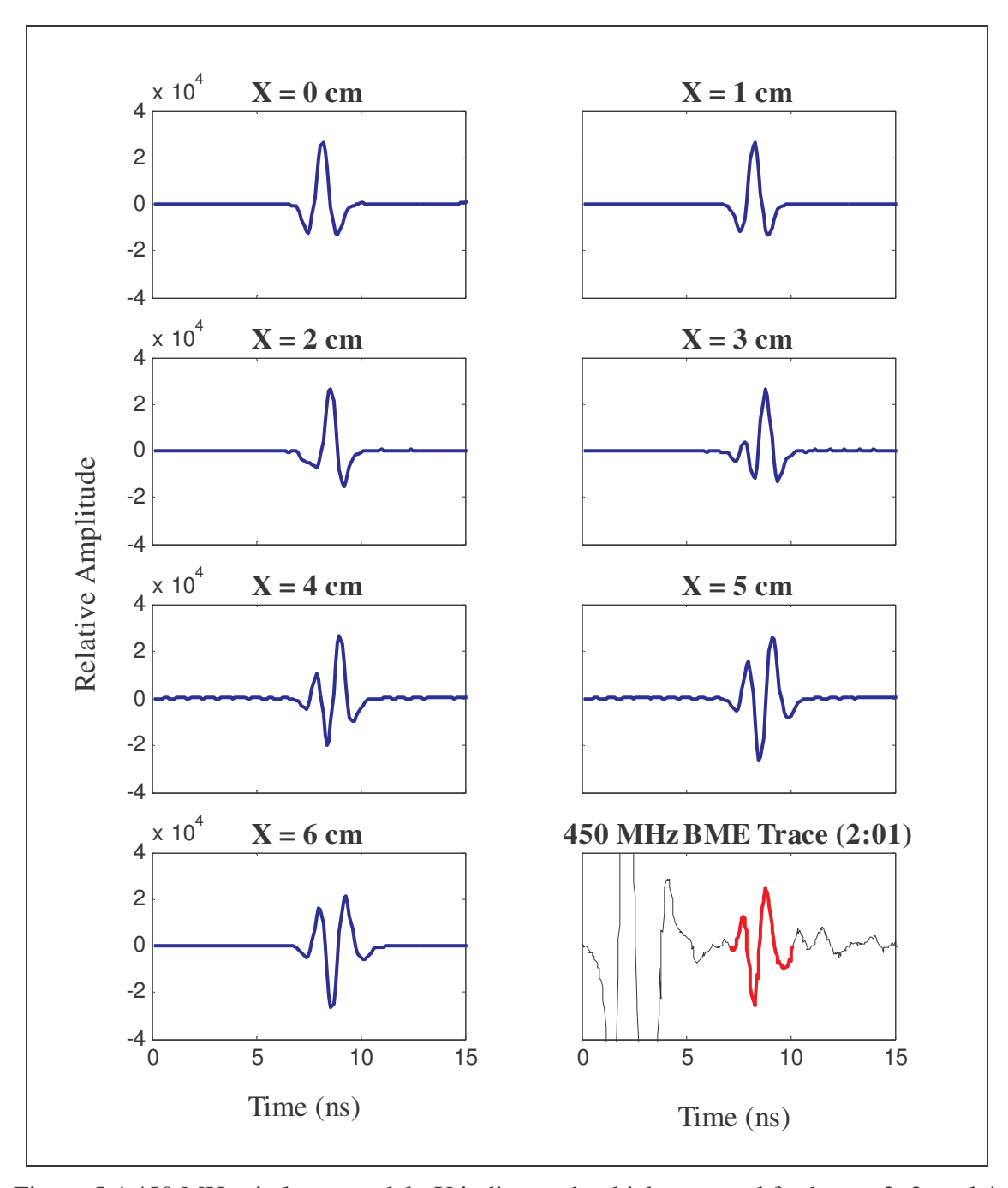


Figure 5.4 450 MHz six layer model. X indicates the thickness used for layers 2, 3, and 4 (ice, air, frozen skin). Notice the evolution of the waveform shape as constructive and destructive interference develops. The last box in the lower right shows the measured BME reflection (red) at 2 hours and 1 minute after burial. Notice how this matches well with the X = 4 model shape.

CHAPTER 6

CONCLUSION

6.1 Discussion

After analyzing the experiment data we learned: 1) the 66 kg (145 lb) BME completely froze (from 38° C to 0° C) over 110 hours while buried in snow with an ambient temperature of -7° C. 2) GPR can effectively locate the BME regardless of core temperature. Figure 6.1 plots the normalized 900 MHz BME reflection waveform negative amplitude minima versus the core temperature. The amplitude was normalized to the temperature data at 8 hours in both offset and range. The waveform amplitude increases during the first 8 hours, and then begins an exponential decline, that matches well with the temperature decline. The increasing amplitude is caused from the evolution of the waveform from "typical" to "unique". At the time of the maximum amplitude, the air pocket and thin layer sequence are completely resolvable with the 900 MHz frequency, at which point the amplitude is related to the core temperature. 3) GPR can uniquely identify man-made objects from natural objects based solely on waveform amplitude comparison. 4) The 900 MHz antenna is able to uniquely identify a body once a 2 cm air pocket (4 cm for the 450 MHz) and associated ice layers have developed by initial body heat melting of snow and subsequent refreezing to ice to produce a unique waveform reflection signature as a result of constructive and destructive interference in the thin layer sequence.

Air pockets develop when an avalanche victim loses heat, melting the snow. All avalanche victims that have been recovered had developed air pockets (Atkins, 2004). The size of the air pocket ranges from millimeters up to 8 centimeters, depending mainly

on how well insulated the victim is. However, the area around the face of a victim usually has the largest gap due to breathing and lack of insulation.

This experiment proved that GPR will be able to locate, image and identify a buried avalanche victim's body while still alive and also after freezing. This opens the door for a prototype to be designed and implemented for search and rescue crews. Currently, there is no user friendly software to help an inexperienced GPR user identify a buried avalanche victim. Locating a buried avalanche victim with GPR requires specialized experience, due to the many variables and the complexity of the problem. Antenna coupling with avalanche debris will also pose a problem, if typical ground coupled antennas are used. The best and most efficient way to map avalanche debris with GPR would be with the use of a helicopter, due to avalanche site access problems and needed response speed. The helicopter could be mounted with a GPR antenna array and be used to map the avalanche debris, locate a positive anomaly, and deploy rescuers. The other option is to have a portable unit that a skier could use to search avalanche debris, similar to a how a transceiver search is performed. If applied correctly, GPR has the potential to save human lives.

Given these results, there are several caveats that need to be mentioned. The first is that the body may not freeze at 0° C due to the salinity and corresponding depressed freezing temperature. The second is that the GPR effects from different types of clothing have not been investigated. The GPR signature may be altered to do the presence of clothing layers and also new materials. The final caveat is that the GPR signature of a human body will most likely be similar to the GPR signature from a deer, elk, or any large mammal found out in the mountain environment. Geometry (size and shape) of the target may be the only way to discriminate the difference between these objects and a human body while using GPR.

6.2 Future Work

The ultimate goal of this research would be to have a GPR system specifically designed for avalanche rescue. The ideal system would have built-in, user-friendly software, so that a non-radar expert could use the system, and be designed with a portable air launched antenna. Designing the antenna will not be an easy task because once a GPR antenna is raised from the ground, multiple problems arise. These problems would include; complex scattering issues, decreased energy penetration, antenna footprint and geometric spreading factors just to name a few. Another problem would be licensing such a rescue device, because the Federal Communications Commission (FCC) has regulated all air launched GPR antennas to be no higher than one meter above the ground. The software would be used to interpret anomalies into a hierarchy of probability including; natural objects, possible targets or man-made objects, and most importantly an actual body. This experimental data could be used as a starting point for developing the software. Once this work is preformed, GPR could some-day save a human life.

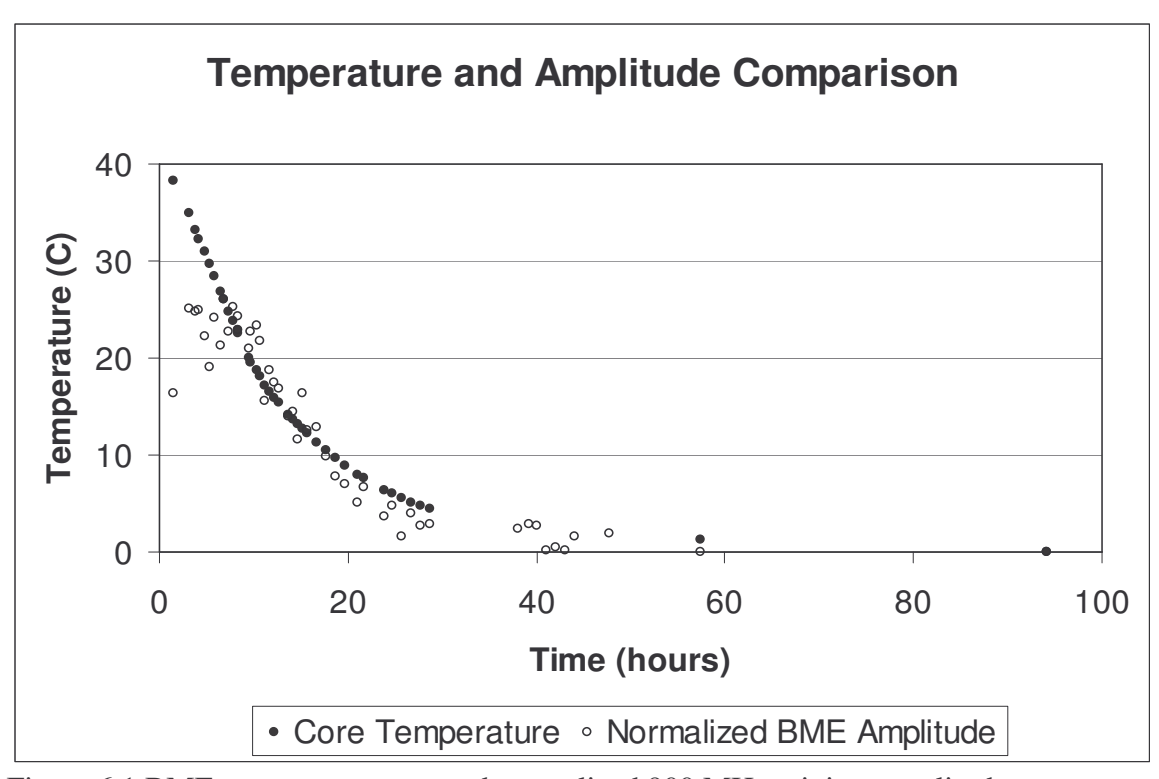


Figure 6.1 BME core temperature and normalized 900 MHz minima amplitude comparison. The amplitude was normalized to the temperature data at 8 hours in both offset and range.

REFERENCES

- Achammer, T., and Denoth, A., 1994, Snow dielectric properties from DC to microwave X-band: Annals of Glaciol., v.19, p. 92-96.
- Annan, A. P., September 2001, Ground Penetrating Radar Workshop Notes, Sensors & Software Inc., Mississauga, Ontario, 192p.
- Annan, A. P., Cosway, S. W., and Sigurdsson, T., June 12-16, 1994, GPR for snow pack water content, *Proceedings of the Fifth International Conference on Ground Penetrating Radar*, Kitchener, Ontario, CA, 465-475.
- Appel 3rd, J. Z., Buhler, L., and Cooper, D. K., 2001, The pig as a source of cardiac xenografts: J. Card. Surg., v.16, n.5, p.345-356.
- Atkins, D., 2004, Colorado Avalanche Information Center: http://geosurvey.state.co.us/avalanche (10-8-04).
- Atkins, D., and Shimanski, C., January 2002, Avalanche Rescue Operation, http://www.mra.org/Avalanche_R2002.pdf, 8-28-03.
- Atkins, D., 1991, Mistakes in Avalanche Rescues, *The Avalanche Review*, Vol. 9, No. 6, April, 11p.
- Avalanche Organization, http://avalanche.org/, (10-8-04).
- Balanis, C.A., 1989. Advanced Engineering Electromagnetics. New York: Wiley. 981p.
- Duke, S. K., 1990, Calibration of ground penetrating radar and calculation of attenuation and dielectric permittivity versus depth: MSc Thesis, Dept. of Geophysics, Colorado School of Mines, Golden, CO, 236 p.

- Durney, C. H., Massoudi, H., and Iskander, M. F., 1986, Radiofrequency radiation dosimetry handbook, 4th ed., USAFSAM-TR-85-73, Brooks Air Force Base, TX, var. pag.
- Frolov, A.D., and Macheret, Y.Y., 1999, On dielectric properties of dry and wet snow, Hydrologodical Processes, Vol. 13, pp 1775-1760.
- Gabriel, C. and Gabriel, S., 1996, Compilation of the dielectric properties of body tissues at RF and microwave frequencies: Final Report AL/OE-TR-1996-0037, AFOSR/NL, Bolling AFB, Washington DC, var.pag.
- Gabriel, C., and Grand, E., H., 1985, Dielectric properties of ocular tissues in the supercooled and frozen states, Physics in Medicine and Biology, Vol. 30, No. 9, pp 975-983.
- Instanes, A., Lønne, I., and Sandaker, K., 2004, Location of avalanche victims with ground-penetrating radar, Cold regions science and technology, V38, pg 55-61.
- Jamieson, B., and Auger, T., 1997, Improved probing for avalanche victims, *SAR Scene Conference*, Sault Ste. Marie, MI, October, 8p.
- McClellan, J. H., Schafer, R.W., and Yoder, M.A., 1999, DSP FIRST a multimedia approach, Prentice Hall, New Jersey, USA, 523p.
- McClung, D., and Schaerer, P., 1993, "The Avalanche Handbook", The Mountaineers, Seattle, WA, 266p.
- Modroo, J., and Olhoeft, G.R., 2004, Avalanche Rescue using Ground Penetrating Radar, *Proc. Tenth Intl. Conf. on Ground Penetrating Radar*, Delft, The Netherlands, June 21-24, 785-788.
- Modroo, J., and Olhoeft, G.R., 2004, Ground Penetrating Radar and Avalanche Rescue, *Proc. International Snow Science Workshop*, Jackson Hole, WY, September 19-24, in press.
- Niessen, J., Kliem, E., Pöhlking, E., and Nick, K.P., 1994, The use of Ground Penetrating Radar to search for persons buried by avalanches: *Proc.Fifth Int'l. Conf. Ground Penetrating Radar*: Kitchener, Ontario, Canada, p.507-517.

- Olhoeft, G. R., 2003, Ground penetrating radar information and GRORADAR: downloadable free from, http://www.g-p-r.com (10-8-04).
- Olhoeft, G. R., 2000, Maximizing the information return from ground penetrating radar: J. Applied Geophys., v. 43, p. 175-187.
- Olhoeft, G. R., 1998, Electrical, magnetic, and geometric properties that determine ground penetrating radar performance: *Proc. Seventh Int'l Conf. Ground Penetrating Radar*: The University of Kansas, Lawrence, KS, USA, p. 177-182.
- Olhoeft, G. R., 1988, Selected Bibliography on Ground Penetrating Radar, SAGEEP proceedings, Golden, CO, March 28-31, p 462.
- Page, D. F., and Ramseier, R.O., 1975, Application of radar techniques to ice and snow studies, Journal of Glaciology, V15 171-191.
- Powers, M. H., 1995, Dispersive ground penetrating radar modeling in 2D: PhD thesis T-4820, Dept of Geophysics, Colorado School of Mines, Golden, CO, 198p.
- Shimanski, Charley: January 2002, Avalanche, http://www.mra.org/avalanche_2002.pdf, 8-21-03.
- Shivola, A., 1999, Electromagnetic mixing formulas and applications: IEE, London, snow: p. 239-244.
- Stern, W., 1929, Versuch einer elektrodynamischen Dickenmessung von Gletschereis: Ger. Beitr.zur Geophysik, v. 23, p 292-333.
- Tremper, B., 2001, Staying alive in avalanche terrain, The Mountaineers Books, Seattle, WA, 284p.
- Ulaby, F.T., Moore, R.K., and Fung, A.K., 1982, Microwave Remote Sensing Active and Passive, Volume 2: Radar remote sensing and surface scattering and emission theory. Reading, MA: Addison-Wesley. p457-1064.
- Utzinger, C., 2002, Report on the meeting of the avalanche rescue commission of IKAR-CISA, Malbun, Lichtestein, 19-24 October 2002, http://www.mra.org, 11p.

- Walter, J., 2003, Avalanche beacons: http://www.gearreview.com (3-18-04).
- Waterworth, P.D., Pig-to-primate cardiac xenotransplantation, The University of Edinburgh http://webex.lib.ed.ac.uk/abstracts/waterw01.pdf (10-28-03) Thesis Abstract
- Wolf, P., Meyer, C., Boudjema, K., Kieny, R., Cinqualbre, J., Jaeck, D., Andre, E., Herrenschmidt, N., and Azimzadeh, A., 1997, The pig as a model in liver xenotransplantation: Vet. Res., v. 28, n.3, p. 217-222.
- Yamaguchi, Y., Maruyama, Y., Kawakami, A., Sengoku, M., and Abe, T., 1991, Detection of objects buried in wet snowpack by an FM-CW radar: IEEE Trans. Geosci. Rem. Sens., v. 29, p.201-208.

APPENDIX

The full Appendix is included on a CD-ROM in a pocket inside the back cover of this thesis. An outline of what is included on the CD is listed in detail below. This thesis is saved on the CD as a *pdf* file. Each Appendix has an individual directory on the CD. The CD also contains *readme.txt* files that outline and give details regarding the context of each directory. This CD is readable on DOS, Windows, Linux, and Macintosh operating systems. To view all the files, you need the following software: Adobe Acrobat, GRORADAR (included), and a picture viewer.

Contents:

- JjM M.Sc. Thesis .pdf.
- Readme.*txt*.

Appendix A

- Raw GPR data and header files, *.dt1 and *.hd files.
- Survey topography files, *.edm.
- Spreadsheet explaining each GPR measurement *.pdf.
- Notebook entries for the experiment *.pdf.
- GRORADAR software.

Appendix B

- Processed data, *.dtz files.
- Image files from GRORADAR (version 2003.11), *.eps files.
- Visual GPR images with annotation, *.jpg files.

Appendix C

- Trace files from raw data, *.bin files.
- Target traces, *.jpg files.
- Notebook entries and procedure notes.

Appendix D

- Documentation for experiment approval.

Appendix E

- Experiment photos, *.jpg files.